



Hydrogen generation during hydrothermal alteration of peralkaline granite

Laurent Truche, Franck Bourdelle, Stefano Salvi, Nicolas Lefeuvre, Apolline Zug, Emily Lloret

► To cite this version:

Laurent Truche, Franck Bourdelle, Stefano Salvi, Nicolas Lefeuvre, Apolline Zug, et al.. Hydrogen generation during hydrothermal alteration of peralkaline granite. *Geochimica et Cosmochimica Acta*, 2021, 308, pp.42-59. 10.1016/j.gca.2021.05.048 . hal-03367692

HAL Id: hal-03367692

<https://hal.science/hal-03367692v1>

Submitted on 6 Oct 2021

HAL is a multi-disciplinary open access archive for the deposit and dissemination of scientific research documents, whether they are published or not. The documents may come from teaching and research institutions in France or abroad, or from public or private research centers.

L'archive ouverte pluridisciplinaire **HAL**, est destinée au dépôt et à la diffusion de documents scientifiques de niveau recherche, publiés ou non, émanant des établissements d'enseignement et de recherche français ou étrangers, des laboratoires publics ou privés.

Hydrogen generation during hydrothermal alteration of peralkaline granite

Laurent Truche^{1*}, Franck Bourdelle², Stefano Salvi³, Nicolas Lefeuvre¹, Apolline Zug¹,
Emily Lloret²

¹ Université Grenoble Alpes, CNRS, ISTERre, F-38058 Grenoble Cedex 9, France

² Univ. Lille, Institut Mines-Télécom, Univ. Artois, Junia, ULR 4515 – LGCgE, Laboratoire
de Génie Civil et géo-Environnement, F-59000 Lille, France

³ Géosciences Environnement Toulouse (GET), CNRS/IRD/UPS/CNES. Toulouse
University, 14 avenue Edouard Belin, 31400 Toulouse

* laurent.truche@univ-grenoble-alpes.fr

Abstract

It is well known that oxidation of ferrous to ferric iron by water can generate molecular hydrogen (H₂), with the most widely recognized natural manifestation being serpentinization of olivine and pyroxene in ultramafic rocks. A less known yet extremely important source of natural H₂ are peralkaline igneous intrusions, where spectacular enrichments of H₂ are documented from fluid inclusions and as free gas migrating through fractured rocks and soils. Of these occurrences, the best studied are those at Strange Lake in Canada, Lovozero and Khibiny in Russia, and Ilímaussaq in Greenland. Based on petrographic observations and fluid inclusions analysis, it has been proposed that the hydrothermal alteration of arfvedsonite, an Fe^{II}-bearing amphibole, is the source of H₂ in this context, although it is yet to be unequivocally demonstrated. To investigate the generation of H₂ during alteration of

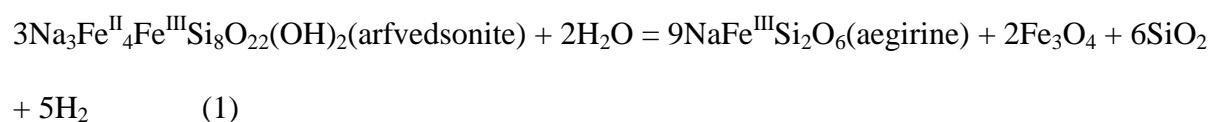
peralkaline granites, we performed hydrothermal experiments on pure arfvedsonite grains and arfvedsonite-bearing granite (10 wt% arfvedsonite) from the Strange Lake pluton (Canada). These materials, in the presence of aqueous solutions, were sealed inside gold capsules or placed within titanium autoclaves, which allowed monitoring H₂ generation in function of temperature (280–400 °C), chlorinity (0 and 3 m NaCl), pH, and starting mineral assemblage. Blank experiments were conducted to quantify the background amounts of H₂ generated from Au/Ti oxidation, diffusing through the reaction cells, release from fluid inclusions or otherwise occluded in minerals. Solids were characterized by XRD, SEM, TEM on FIB foils, and STXM-XANES. Outcomes of this study demonstrate the production of H₂ in agpaitic peralkaline rocks by the hydrothermal alteration of arfvedsonite. The rate of H₂ production, normalized to the specific surface area of arfvedsonite, increases with temperature from 1100 to 2200 pmol cm⁻² day⁻¹ between 280 and 400 °C, respectively. Chlorinity tends to have a negative impact on the reaction rate, while circumneutral to alkaline conditions clearly promote H₂ generation. Altering whole granite samples instead of arfvedsonite grains only also enhances H₂ production rate. The presence of aluminum, released from microcline and albite dissolution, may increase both the solubility and the dissolution rate of arfvedsonite by promoting precipitation of phyllosilicates. At least two different types of phyllosilicates were observed, chlorite and montmorillonite. Magnetite and secondary zircon were also identified at the surface of reacted arfvedsonite (Zr content = 1200 ppm). The H₂ production rates reported here at 280–400 °C are comparable, and even faster than those documented for serpentinization of olivine and harzburgite. A major feature of arfvedsonite alteration in peralkaline plutons is the formation of aegirine as a replacing mineral. However, aegirine was never observed in the reacted solids from our experiments, under the condition tested (up to 400 °C and 400 bar). This may be an effect of pressure, oxygen fugacity, or reaction progress, parameters that remain to be investigated to better constrain the reaction mechanism of

49 arfvedsonite alteration. Agpaitic peralkaline igneous intrusions thus represent a fertile
50 geological setting for deep microbial subsurface ecosystems, abiotic synthesis of organic
51 molecules, and natural H₂ exploration for an alternative source of energy.

1. Introduction

Production of molecular hydrogen (hereafter hydrogen or H₂) is a phenomenon that can occur naturally during water-rock interaction (Klein et al., 2020). Recently, this process has drawn increasing scientific attention owing to the central role that this molecule plays in supporting deep microbial subsurface ecosystems and in promoting abiotic synthesis of organic molecules (Ménez et al., 2020; Sleep et al., 2004; Truche et al., 2020). Furthermore, in the last couple of years, growing pressure on our society to develop carbon-free technology has sparked an unprecedented interest in naturally occurring H₂, as it could represent a potential alternative resource to fossil fuels (Donzé et al., 2020; Gaucher, 2020; Murray et al., 2020; Prinzhofer et al., 2018; Truche and Bazarkina, 2019, Smith et al., 2005). Spontaneous production of H₂ in nature involves nonbiological processes in the Earth's crust, driven by reactions such as (1) reduction of water during the oxidation of iron in minerals (Klein et al., 2013, McCollom et al., 2016; McCollom et al., 2020a; Milesi et al., 2015), (2) radiolysis of water due to radioactive decay of U, Th, and K (Lin et al., 2005; Truche et al., 2018), (3) reaction of water with surface radicals during mechanical fracturing of silicate-bearing rocks (Hirose et al., 2011), and (4) reaction of FeS with water to generate FeS₂ plus H₂ (Drobner et al., 1990). Among these reactions, the most thoroughly investigated has been undoubtedly those taking place during hydrothermal alteration of ultramafic rocks (i.e. serpentinization), where hydration of Fe^{II}-bearing olivine and pyroxene leads to the concomitant reduction of water into H₂ (Cannat et al., 2010; Klein et al., 2020; Worman et al., 2016, 2020). The numerous occurrences of H₂-bearing fluids documented in ultramafic geological environments such as mid-oceanic ridges (Charlou et al., 2002; Seewald et al., 2003), ophiolites (Chavagnac et al., 2013; Coveney et al., 1987; Neal and Stranger, 1983; Vacquand et al.; 2018), Precambrian terrains or greenstone belts (Boreham et al., 2021; Sherwood Lollar et al., 2014) have of course motivated these researches.

Less known than the above-mentioned geological contexts, high H₂ contents are also reported in olivine free, agpaitic peralkaline igneous intrusions among which those of Strange Lake (Canada), Ilímaussaq (Greenland), Lovozero and Khibiny (Kola Peninsula, Russia) are world-class occurrences (Krumrei et al., 2007; Marks and Markl, 2017; Nivin, 2019; Potter et al., 2013; Salvi and Williams-Jones, 1992, 2006). In the latter two cases, H₂, together with CH₄ and higher hydrocarbons, in addition of being observed in fluid inclusions entrapped in minerals (up to 40 mol%), also occurs as a free gas phase in fracture networks in the rocks, as well as in underground mine galleries where it poses serious safety issues (Ikorskiy, 1986; Nivin, 2016, 2019, 2020; Nivin et al., 1995; 2001). Such unique occurrences of H₂ occluded in minerals, diffusely dispersed and freely migrating in rock fractures and soils, raise important questions about the source of this gas. The two main processes that have been proposed to account for H₂ production in these rocks rely either on early magmatic degassing (Beeskow et al., 2006; Konnerup-Madsen, 2001; Vasyukova et al., 2016; Vasyukova and Williams-Jones, 2019) or on late subsolidus hydrothermal alteration of ferrous minerals (Salvi and Williams-Jones, 1992, 1997; Potter and Konnerup-Madsen, 2003; Potter et al., 2013; Vasyukova et al., 2016; Vasyukova and Williams-Jones, 2019). The latter hypothesis is supported by fluid-inclusion evidence and by the petrographic observation of pseudomorphic replacement of the Fe^{II}-bearing amphibole arfvedsonite by aegirine, a Fe^{III}-bearing pyroxene, as shown in **Figure 1**. Such a reaction may lead to H₂ production according to:



At Strange Lake, this reaction is interpreted to have been caused by relatively saline orthomagmatic brines released during crystallization of the transsolvus granite at T ≥ 350 °C (e.g. Salvi and Williams-Jones, 1992; 1996, 1997).

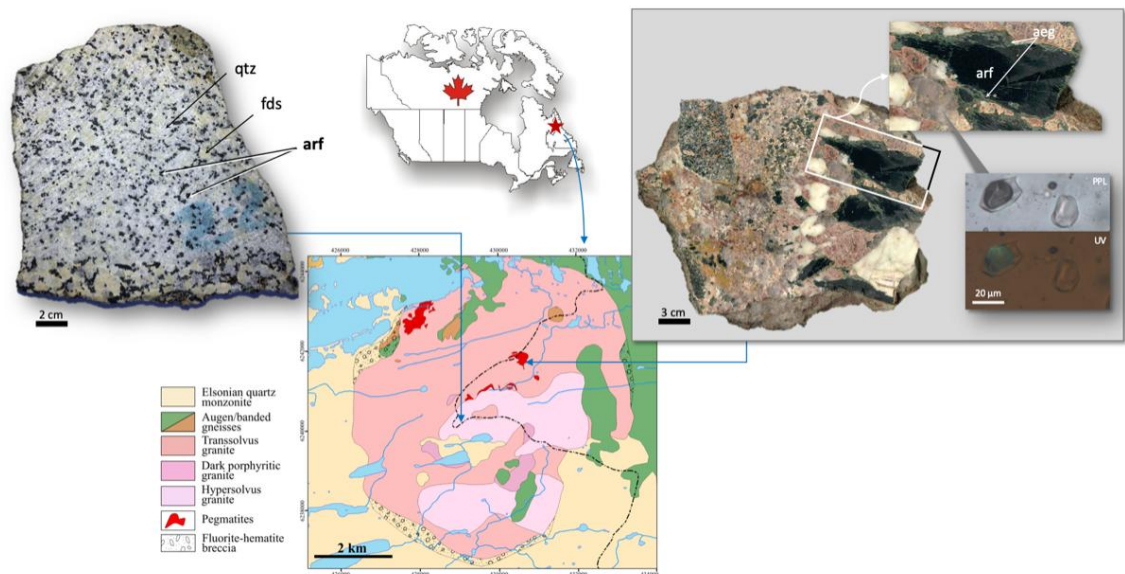


Figure 1. Geological map of the Strange Lake pluton (courtesy of O. Vasyukova) locating the sample of hypersolvus granite used for the experiments (left-hand side). On the right-hand side is shown a sample of altered pegmatite where incipient replacement of arfvedsonite (large dark green crystals) by aegirine (light green) is clearly visible. The fluid inclusions displayed in the inset represent an example of coexisting L- and V-rich individuals, where the latter contain hydrogen as well as higher-order hydrocarbons, showing fluorescence under UV illumination. qtz = quartz, fds = feldspars, arf = arfvedsonite, aeg = aegirine.

Recently, Vasyukova et al. (2016), and Vasyukova and Williams-Jones (2019)

documented in more details the fluid evolution of the hydrothermal systems at Strange Lake, on the basis of a meticulous fluid and melt inclusion study. According to these authors, fluid evolution commenced with the exsolution of a brine (~25 wt% NaCl eq.) coexisting with an immiscible CH₄-dominant vapor from a pegmatitic melt, at temperatures of ~450–500 °C and a pressure of ~1100 bar. During isobaric cooling path, the vapor phase gradually evolved from CH₄-dominant to a CH₄-bearing mixture with a significant proportion of H₂ and higher-order hydrocarbons. Formation of C₂ to C₆ hydrocarbons, and at least part of the hydrogen, was synchronous to the alteration of arfvedsonite to aegirine and occurred at ~325–360 °C. The last stage of fluid evolution – after cessation of arfvedsonite alteration – is characterized by a CO₂-dominant fluid at ~300 °C. Along this temperature-pressure paths, the apparent

salinity of the aqueous fluid decreased from ~25 to ~4.5 wt% NaCl eq. due to fluid-rock interaction.

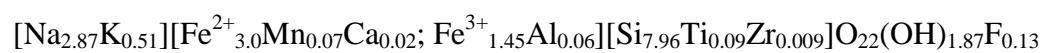
Based on this knowledge, we constructed an experimental study that, for the first time, reproduces the production of H₂ by altering arfvedsonite from peralkaline granite. As starting material, we used separate arfvedsonite grains and whole granite samples from the Strange Lake pluton and, by controlling temperature, pH and salinity of the fluid we obtained the amounts, rate and mechanisms of H₂ generation between 280 and 400 °C at various pressures. These results are compared to available experimental data on H₂ generation during serpentinization of olivine and ultramafic rocks. Our findings provide new, important insights into H₂ generation during the interaction of aqueous fluids with peralkaline rocks.

2. Experimental Methods

2.1. Materials

A sample of unaltered peralkaline granite from Strange Lake (Canada), hereafter noted SL-granite, was used as a starting material for all experiments (**Fig. 1**). This granite, of hypersolvus composition, represents the earliest and least evolved intrusive facies of the pluton (Siegel et al., 2018). The sample was collected from an outcrop in the southern parts of the pluton, a unit known to be unattained by hydrothermal alteration (e.g. Salvi & Williams-Jones 1990; Siegel et al., 2018). Attention was also paid to eliminate all parts that were exposed to weathering. The unaltered nature of the sample was verified by petrographic observations. The modal mineralogical composition of SL-granite, deduced by X-Ray diffraction (XRD) analysis, is as follows: 33 ±2 wt% albite, 28 ±2 wt% microcline, 28 ±2 wt% quartz, 10 ±2 wt% arfvedsonite, 0.6 ±0.2 wt% fluorite, and minor rutile. Aegirine was neither detected by XRD analysis nor by any other technique used in this study.

The SL-granite sample was ground with an agate mortar, sieved (53–212 μm), sonicated in Milli-Q water (resistivity of 18.2 M Ω .cm at 25 °C) to remove adhering fine particles, and dried in a glove box under inert argon atmosphere ($[\text{O}_2] < 1 \text{ ppm}$) at room temperature. Arfvedsonite and quartz were recovered separately using a hand magnet and hand-picked under a binocular microscope, respectively. Quartz was used in some blank experiments to evaluate possible sources of H_2 . Once separated, the solids were washed with 1 M HCl, rinsed several times with Milli-Q water and stored under anoxic conditions (using Ar gas) in a glove box ($[\text{O}_2] < 1 \text{ ppm}$). The chemical composition of arfvedsonite was obtained by electron microprobe analysis (**Supplementary Table S1**) and its $\text{Fe}^{3+}/\text{Fe}^{2+}$ ratio was measured by Scanning Transmission X-Ray microscopy (STXM - see analytical methods below). Based on these data and using the methods proposed by Li et al. (2020), we obtained the following arfvedsonite formula:



The BET surface areas of SL-granite and arfvedsonite measured using Kr as the adsorbate gas are similar: $0.30 \pm 0.03 \text{ m}^2 \text{ g}^{-1}$.

2.2. Experiments

2.2.1. Experimental Strategy

Initially, we performed a number of blank experiments to ensure that all hydrogen measured was produced from the experimental charges, and, conversely, that no hydrogen escaped the experimental systems. More details on blank runs are provided in subsequent sections. To test the potential effect of minerals other than arfvedsonite, in addition of using arfvedsonite-only powders we also ran experiments using whole SL-granite. Experiments were carried out at 280 to 400 °C, in order to cover the expected temperature range at which arfvedsonite is

interpreted to be replaced by aegirine in nature (Salvi and Williams-Jones, 1992; 1996, 1997, 2006; Potter et al. 2013). For similar reasons, the pressure during the experiments ranged from 70 to 500 bar. A parametric investigation of the effect of pH and salinity was performed at 350 °C and 500 bar. A salinity of 3 m NaCl (i.e. 17.4 wt% NaCl) was chosen to reproduce those measured in fluid inclusions (Vasyukova et al., 2016). Finally, as the pH of the fluids responsible for the alteration of the Strange Lake granite was quite variable (i.e., ranged from 3 to 10; Vasyukova and Williams-Jones, 2019), we investigated very contrasted pH conditions using 0.1 m HCl (pH = 1) or 0.1 m NaOH (pH = 13) starting solutions. The pH value was free to evolve over the course of the experiments but, regardless, such acidic or alkaline solutions impose drastically different pH conditions.

Two experiments were designed to measure the rate of H₂ production during SL-granite alteration. One experiment was carried out at 280 °C and 70 bar, in the presence of SL-granite and pure water. Another experiment, performed at 350 to 400 °C, was designed to study the effect of salinity and fluid density on H₂ production rate. This experiment aimed at reproducing the vapor-liquid immiscibility that occurs when adiabatically decompressing a supercritical brine from 400 °C/400 bar to 400 °C/260 bar. The sections below detail the experimental setups and conditions.

2.2.2. Experiments performed at 350°C/500 bar in gold capsules

A set of 17 experiments were carried out in gold capsules loaded in cold-seal pressure vessels and reacted at 350 °C and 500 bar for 15 days (360 hours) (runs #1 to #15 in **Table 1**). The experimental charges consisted of ~50 mg of solids (SL-granite, arfvedsonite, or quartz) and ~50 mg of solution (milli-Q water, or 3 m NaCl brines ± 0.1 m HCl ± 0.1 m NaOH). Blank experiments without solid (fluid only) or without fluid (solid only) were performed to quantify possible background H₂ generation due to Au capsule oxidation, or released from

minerals. The Au capsules (volume of ~0.2 mL) were filled under anoxic condition inside a glove box under Ar atmosphere ($[O_2] < 1$ ppm), and their extremities were pinched shut before extracting them out of the glove box. The capsules were then immediately welded and placed inside an oven at 90 °C overnight to ensure absence of leakage (the mass of the capsules was weighted before and after heating). For the experiment, the capsules were loaded into a cold-seal pressure vessel filled with water as the pressure medium, pressurized at 500 bar and heated to 350 °C for 15 days. After reaction, the autoclaves were quenched with a flux of compressed air for up to 15 minutes and opened. The Au capsules were weighted again to verify leakage had not occurred. A syringe equipped with an indenter and a three-way valve was used to pierce the Au capsules and to release the produced gas. The syringe was previously flushed with Ar to remove air. The gas mixture (Ar + released gases) was sampled through a septum placed on one of the valve's taps and analyzed by gas chromatography for H_2 , CO_2 and CH_4 . All details of gold capsule piercing, gas recovery and analysis are described by Malvoisin et al. (2013). The pH and chemical composition of the reacted fluids were not measured in these experiments because of the difficulty in retrieving sufficient amount of fluid after capsule piercing and gas analysis. The solids were recovered and immediately transferred into the anoxic glove box where they were rinsed with milli-Q water, dried at ambient temperature under Ar atmosphere and stored until the time of analysis.

214 **Table 1:** List of experiments and conditions.

#run	Initial fluid composition	Starting material	Experimental setup	T (°C)	P (bar)	W/R mass ratio
1	- (dry)	SL-granite	gold capsule	350	500	no solution
2	- (dry)	arfvedsonite	gold capsule	350	500	no solution
3 and 3'	H ₂ O	SL-granite*	gold capsule	350	500	1
4 and 4'	H ₂ O	arfvedsonite*	gold capsule	350	500	1
5	H ₂ O	no solid	gold capsule	350	500	no solid
6	3 m NaCl	SL-granite	gold capsule	350	500	1
7	3 m NaCl	arfvedsonite	gold capsule	350	500	1
8	3 m NaCl	quartz	gold capsule	350	500	1
9	3 m NaCl	no solid	gold capsule	350	500	no solid
10	3 m NaCl + 0.1 m HCl	SL-granite	gold capsule	350	500	1
11	3 m NaCl + 0.1 m HCl	arfvedsonite	gold capsule	350	500	1
12	3 m NaCl + 0.1 m HCl	no solid	gold capsule	350	500	no solid
13	3 m NaCl + 0.1 m NaOH	SL-granite	gold capsule	350	500	1
14	3 m NaCl + 0.1 m NaOH	arfvedsonite	gold capsule	350	500	1
15	3 m NaCl + 0.1 m NaOH	no solid	gold capsule	350	500	no solid
QTZ280	H ₂ O	Quartz	Ti autoclave	280	70	20
SL1	H ₂ O	SL-granite	Ti autoclave	280	70	20
SL9	H ₂ O	SL-granite	flexible-cell autoclave	350 → 400	400 → 260	10

215 “*” indicates that the experiment was replicated, “m” stands for molality in mol kg_w⁻¹

216

217 2.2.3. Experiments performed at 280 °C in a batch autoclave

218 Two experiments were conducted in a 450-mL Parr® stirred batch hydrothermal

219 reactor made of pure titanium (Ti grade 4). The reactor was equipped with several

220 connections that enable periodic on-line sampling of reaction liquid (Ti sampling line fitted

221 with a 1 µm Ti porous filter) and gas, to monitor reaction progress. The autoclave was heated

in air at 400 °C for 48 hours to make sure all surfaces were oxidized prior to the experiment to form a quasi-inert TiO₂ passivated layer. The investigated system was composed of 300 g of Milli-Q water and 15 g of powdered (53–212 µm) SL-granite (#SL1) or pure quartz (#QTZ280), for an initial water-to-rock mass ratio (W/R) of 20 (**Table 1**). The experiment conducted with pure quartz was used as a blank to monitor background H₂ production from eventual autoclave corrosion or fluid inclusion decrepitation. The reaction vessel was bubbled and flushed with Ar to ensure anoxic condition prior to heating. The reactor was then rapidly heated to 280 ± 1 °C within 15 min. The experiments were conducted at 70 bar total pressure and 280 °C, during 4 weeks. This pressure resulted from the vapor pressure (64 bar at 280 °C) plus the background Ar pressure that ensured anoxic condition and leakage detection during the run. The calculated partial pressures of H₂, CO₂ and CH₄ produced during the experiment remained < 0.2 bar during the entire run.

Liquid and gas were sampled regularly throughout the experiments. During each sampling, three separate liquid aliquots were collected for a total volume of ~6 mL. The first aliquot allowed purging of the sampling line. The second aliquot was used for pH measurements. Total dissolved cations (Ca, Na, K, Mg, Al, Si, Fe, Mn) were determined from the third aliquot, after filtration at 0.2 µm and HNO₃ dilution. Gas was sampled directly into a gas-tight, Ar-purged glass syringe and analyzed by gas chromatography for the abundance of H₂, CO₂ and CH₄. Each successive sampling induced a slight pressure decrease – from 70 to 66 bar over the entire duration of the experiments. Necessary corrections were made to calculate the total amount of H₂ produced by considering the volume of liquid and gas sampled, the remaining volume of liquid or gas in the reactor at each step, and the pressure change. The amount of H₂ dissolved in the aqueous phase was calculated using the Henry's law constant at water saturation pressure reported by Fernández-Prini et al. (2003): $\text{Log}_{10}(k_H/\text{MPa}) = 1.88$ at 280 °C and P_{sat} . After reaction, the autoclave was quenched in cold

water and opened. Solids were immediately transferred into a glove box, rinsed with Milli-Q water and then dried at room temperature.

2.2.4. Experiments performed at temperatures ranging from 350 to 400 °C in a flexible-cell hydrothermal autoclave

One experiment (#SL9) was carried out in a flexible-cell hydrothermal apparatus (CoreTest®) using a 155 mL flexible titanium reaction cell fitted with a titanium sampling line (1 µm Ti porous filter, Ti tube and valve). All titanium components were heated in air for at least 48 hours at 400 °C prior to the experiment in order to form a relatively inert TiO₂ surface layer. The reaction cell was contained within a stainless-steel pressure housing, with water used as an external pressurizing fluid. The external pressurizing water was spiked with 1 mmol L⁻¹ SrCl₂, and the concentration of Sr inside the flexible Ti cell was monitored over the course of the experiment to test for leakage. The reaction cell was initially loaded with 7.3 g of SL-granite of uniform grain size (53–212 µm) and 73 g of Milli-Q water - W/R = 10 (**Table 1**). Fluids were sampled during the experiments in order to monitor reaction progress over time. At each instance, two separate aliquots were sampled for a total mass of fluid of 3 to 7 g. The first one corresponded to the sampling of the purge line and the second one was used for gas and total dissolved cation analysis. These samples were collected in two separate titanium cells previously evacuated (primary vacuum). The pressure was returned to the targeted value after each sampling point. This experiment consisted of 3 consecutive stages: 1) 350 °C and 400 bar, for 336 hours; 2) 400 °C and 400 bar, for 216 hours; and finally 3) 400 °C and 260 bar, after NaCl-bearing solution injection, for 210 hours. During the first two stages of the experiment (up to 400 °C and 400 bar), the reaction occurred in a single-phase fluid. The flexibility of the Ti reaction cell allowed fluids to be sampled without loss of pressure and eliminated the presence of a vapor headspace so that reactions remained

confined to the aqueous phase. The density of the fluid decreased slightly, from 0.67 to 0.62 g cm⁻¹, from stage 1 to stage 2 (single-phase fluid). In contrast, the last stage was conducted in the presence of two fluid phases: brine and vapor. Ten milliliters of a 5 molar NaCl brine were injected inside the Ti flexible cell at 400 °C and 400 bar by means of a high-pressure hand (capstan) pump. After brine injection, the pressure decreased to 260 bar, inducing phase separation. The respective density, volume and salinity of the brine and vapor phases were as follow: 0.70 g cm⁻¹ / 16 mL / 2.7 m NaCl, and 0.19 g cm⁻¹ / 89 mL / 0.028 m NaCl. During this last stage, only the vapor phase was sampled to avoid damaging the flexible cell and strong fluctuations of the W/R ratio. After reaction, the autoclave was quenched with a flux of compressed air for up to 20 minutes and opened. Solids were immediately transferred into the glove box, rinsed with Milli-Q water and then dried at room temperature.

2.3. Analytical techniques

2.3.1 Gas and liquid analysis

The gas samples were analyzed using a Perkin Elmer® CLARUS 500 gas chromatograph (GC) equipped with a thermal conductivity detector (TCD) and a 2-m long column (RESTEK® Shin Carbon ST 80/100) traversed by Ar as carrier gas. The GC was calibrated using several Ar+H₂+CH₄+CO₂+CO gas mixtures of different concentrations injected with a gas syringe of calibrated volume. The estimated analytical error is ± 5 %. In most cases the reported H₂, CO₂ and CH₄ concentration are averages of 3-4 gas injection into the GC. For comparative purposes, the measured H₂ concentrations were normalized to the total number of moles of H₂ generated per gram of SL-granite or arfvedsonite to account for variations in the amount of solid reactants used in different experiments and for the changing mass of fluid present in the reaction vessel as aliquots are removed during sampling.

Liquid aliquots from experiments carried out in Ti autoclaves (both Parr and Coretest) were filtered (0.2 μm), diluted and acidified (2 vol. % HNO_3), and analyzed for major cations with matrix-matched standards using inductively coupled plasma-atomic emission spectroscopy (ICP-AES; Varian® 720ES) with a precision of 3 % at the 95 % confidence level. Fluid chemistries as analyzed and corrected for acid dilution are reported in **Supplementary Tables S2**.

2.3.2. *Electron microscopy*

Scanning Electron Microscopy (SEM) was used for examination of the morphology and texture and for chemical investigation of the powdered samples before and after reaction. SEM images were obtained using a Tescan® Vega3 electron microscope operating at 15 kV, equipped with an Energy Dispersive X-ray Spectrometer (EDXS). Photomicrographs were recorded both in secondary (SE) and backscattered (BSE) electron modes.

Additional compositional data were obtained by Electron Microprobe Analysis (EMPA) using a JEOL® JXA 8230 electron microprobe equipped with five wavelength-dispersive spectrometers. Arfvedsonite was analyzed with an accelerating voltage of 15 kV, a beam current of 12 nA and a defocused beam diameter of 5 μm . The standardization was made using natural minerals and synthetic oxides standard set (P&H Developments Ltd.). The Smithsonian hornblende USNM143965 (Jarosewich et al., 1980) was measured as an unknown together with our samples to verify analytical accuracy and precision.

Transmission Electron Microscopy (TEM) micrographs and Energy-dispersive X-ray (EDX) analysis were obtained on thin section cut with a Focused Ion Beam (FIB). The areas of interest were milled with a FIB in order to obtain ultrathin samples – with conservation of the texture of the mineral phases – transparent to the TEM electrons. This was done on a cut oriented vertically and perpendicular to the sample surface, using the FEI strata DualBeam

235 of Institut d'Electronique, de Microélectronique et de Nanotechnologie (IEMN, Lille), and cut out to a size of approximately 15 μm by 5 μm and a thickness around 80 nm. Such preparation allows a cross sectional view of the altered material. To check the preservation of the mineral crystalline structure after FIB milling, lattice-fringe imaging was systematically carried out with the TEM, following the protocol of Bourdelle et al. (2012). The FEI Tecnai® G2-20 model TEM used (Plateforme de Microscopie Electronique de Lille (PMEL) – Institut Chevreul of Lille, France) operates at 200 kV, and is equipped with a Charged-Coupled Device (CCD) camera and an EDX spectrometer allowing to acquire chemical analysis (on 50 nm diameter surface area) with a counting time of 30 s for a dead time of less than 10 %.

2.3.3. X-ray diffraction

Powder X-ray diffraction (XRD) patterns were acquired from both random and oriented mounting of the samples. The diffractometer was a Bruker® D8 equipped with a SolX Si(Li) solid state detector from Baltic Scientific Instruments using $\text{CuK}\alpha$ radiation ($\lambda = 1.5406 \text{ \AA}$) generated at 40 kV and 40 mA. On the primary side, a divergence slit (0.298°) and a soller slit (2.5°) were used, while on the secondary side an antiscattering slit (0.298°), a soller slit (2.5°) and a receive slit (0.06°) were used. Intensities were recorded at $0.026^\circ 2\theta$ step intervals from 5 to 90° (5 s counting time per step) and from 2 to 50° (4 s counting time per step) for bulk and clay mineralogy determination, respectively. The bulk mineralogy was determined on the $<2 \text{ mm}$ fraction (obtained after grinding the samples using a McCrone® micronizing mill). The clay mineralogy was determined on the $<2 \mu\text{m}$ fraction. Following sonication of the samples, this fraction was extracted by centrifugation. Oriented mounts were prepared by drying the resulting suspension onto glass slides. Ethylene-glycol (EG) solvation of the slides was achieved by exposing them to EG vapor at 50°C for a minimum of 12 h. Estimates of modal abundance of minerals were performed using the Rietveld refinement

method using the BGMN computer program (www.bgmnn.de), based on the XRD patterns collected on randomly oriented samples.

2.3.4. STXM-XANES

X-ray adsorption near-edge structure spectroscopy (XANES) data were acquired using the Scanning Transmission X-ray microscope (STXM) of the PolLux beamline (for details about the beamline, see Raabe et al., 2008) at the Swiss Light Source (Paul Scherrer Institute – SLS, Switzerland) and the HERMES beamline (Belkhou et al., 2013) at the SOLEIL synchrotron (France). During data collection, the SLS and SOLEIL synchrotron storage rings operated at 2.4 GeV / 400 mA current and 2.75 GeV / 450 mA current, respectively. STXM allows to collect XANES data on crystallites with a thickness < 100 nm to allow X-ray transmission. The thin crystallites of arfvedsonite were recovered in each reaction product, and dispersed in ethanol; a drop of which is placed (then evaporated) on a carbon holey support film placed on a TEM 200 mesh copper grid. Stacks of images were obtained by scanning – with a spatial resolution of 30 nm – the area of interest in the x–y direction over the 700–730 eV energy range (Fe L_{2,3}-edge). Each image of a stack was recorded at one energy, so that the compilation of the same pixel on each image gives one spectrum. Spectra were extracted from stacks using the aXis2000 software (Hitchcock, 2012) and processed following the protocol of Bourdelle et al. (2013). Data were recorded using a circularly polarized light and a dwell time per pixel and energy point of 10 ms.

Spectra acquired through the Fe L_{2,3}-edge energy range were used to estimate the Fe³⁺/ΣFe ratio with an uncertainty around 5 %. This estimate of Fe³⁺/ΣFe ratio is extracted from the ratio of the two (L₃-b and L₃-a) major peak intensities, following the calibration of Bourdelle et al. (2013). This calibration was established on standard samples, all silicates: five iron-silicate glasses (containing various Fe³⁺ contents), eight phyllosilicates (several chlorites,

371 micas and smectite with various Fe^{3+} contents) and a fayalite. This calibration is not
372 dependent on the silicate structure. To evaluate the result reproducibility, 2 or 3 crystallites of
373 each sample were analyzed, and for each of them 2 to 3 spectra were extracted (i.e. 4 to 6
374 spectra per sample).

376 3. Results

377 3.1 H_2 generation from alteration of peralkaline granite and of pure arfvedsonite at 350 °C, 378 500 bar

379 A total of 15 experiments were carried out in gold capsules at 350 °C and 500 bar
380 during 15 days (360 hours) in order to evaluate the effect of both pH and salinity on H_2
381 generation from peralkaline granite and pure arfvedsonite hydrothermal alteration. Some of
382 these experiments were replicated twice to ensure good reproducibility of the measurements
383 (**Table 1, Fig. 2**). As for potential H_2 loss, the very low H_2 permeability of gold below 350 °C
384 has been previously demonstrated (Chou, 1986; Malvoisin et al., 2013). Particular attention
385 was paid at evaluating blank conditions of our experiments, *i.e.*, test whether H_2 could be
386 produced from oxidative dissolution of the gold capsules, fluid inclusion decrepitation, or by
387 releasing of gases occluded in the minerals. We therefore designed a series of runs to
388 determine possible background blank values. The total amounts of H_2 produced during blank
389 experiments are shown in **Figure 2a**.

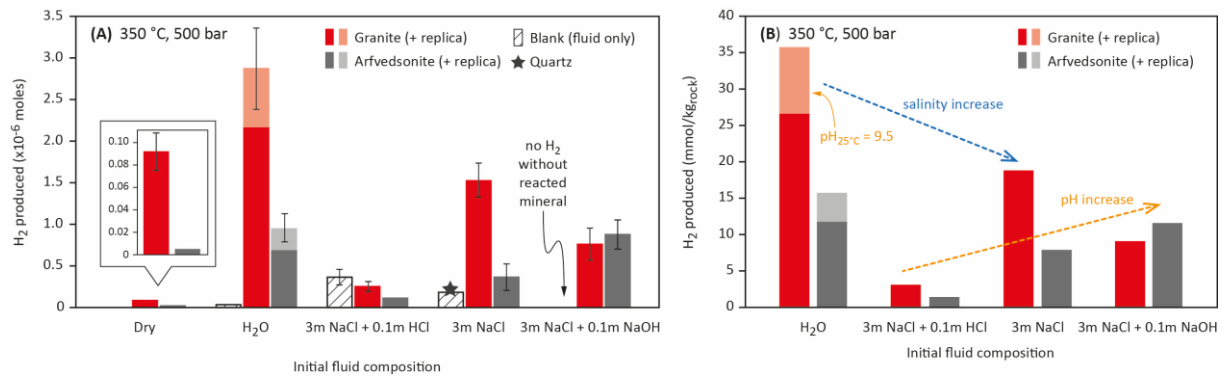
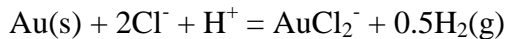


Figure 2. Production of H₂ after 360 hours elapsed time in the gold capsule experiments carried out at 350 °C and 500 bar. Different initial fluid compositions were tested to evaluate the effect of pH and salinity. (a) Experiments carried out in the presence of SL-granite (red) or arfvedsonite (black) are compared to the blanks: fluid only (dashed lines) or quartz + 3 m NaCl (grey star). The notation “dry” indicates that the gold capsule was loaded with solid material only (no fluid). The 2 replicates performed in the presence of water + SL-granite or arfvedsonite are shown in light red and light grey, respectively. (b) Production of H₂ normalized to the mass of solids (SL-granite or arfvedsonite) as a function of fluid composition. Error bars reflect the cumulative uncertainty associated with measuring the volume of gas released after piercing the gold capsules and with the analytical uncertainty.

Hydrogen production from gold capsule oxidative dissolution (Equation 2) was measured as a function of pH in a 3 m NaCl brine (no solid loaded in the capsule).



The amount of H₂ produced by gold dissolution increased when pH decreased. The concentration of dissolved hydrogen was below the detection limit under alkaline condition (0.1 m NaOH + 3 m NaCl), but reached $8.6 \pm 0.2 \times 10^{-4}$ m at 350 °C and 500 bar in 0.1 m HCl + 3 m NaCl solution. Such a concentration is in very good agreement with thermodynamic predictions using the HCh software (Shvarov, 2008), based on the stability constant reported by Stefansson and Seward (2003) for the chloridogold(I) complex ($m_{\text{H}_2(\text{aq})} = 6.3 \times 10^{-4}$ m at 350 °C and 500 bar in equilibrium with native Au in a 0.1 m HCl + 3 m NaCl solution).

Under acidic condition, H₂ production recorded during SL-granite and pure arfvedsonite hydrothermal alteration experiments was so low that it can be simply explained by the oxidative dissolution of the gold capsule alone (**Fig. 2a**). However, under

circumneutral to alkaline conditions, H₂ produced by gold dissolution represents only a negligible fraction of the total amount of H₂ generated during hydrothermal alteration of SL-granite and pure arfvedsonite (**Fig. 2a**).

Blank experiments performed under dry condition (powdered SL-granite or arfvedsonite loaded without water in the gold capsules), or only with quartz from SL-granite reacted with 3 m NaCl brine, revealed that the release of pre-existing H₂ from gases occluded in the minerals or entrapped in fluid inclusions is also negligible. Indeed, less than 5 % of the total amount of H₂ produced in the experiments where SL-granite or pure arfvedsonite were hydrothermally reacted can be attributed to pre-existing H₂.

To better compare the effect of pH, salinity and mineralogical assemblage, the total amounts of H₂ produced during both SL-granite and arfvedsonite-bearing experiments were normalized to the mass of solid initially introduced inside the gold capsules (**Fig. 2b**). Clearly, H₂ production was promoted by circumneutral to alkaline conditions. The maximum amount of H₂ produced was recorded after reaction of SL-granite with water: from 27 to 36 mmol kg_{rock}⁻¹ of H₂ were produced within 15 days (**Fig. 2b**). Note that hydrothermal alteration of SL-granite naturally imposes alkaline conditions (pH_{25°C} = 9.5 and 8.2 were measured after runs #SL1 and #SL9 carried out at 280 °C and 400 °C, respectively - see below). Altogether, these experiments demonstrated that H₂ production from the hydrothermal alteration of SL-granite and of pure arfvedsonite strongly depends on pH. The comparison of experiments conducted with and without dissolved NaCl reveals that salinity decreases the production of H₂, by 10 to 40 %. Comparatively, SL-granite alteration produced more H₂ than arfvedsonite alone.

Carbon dioxide and CH₄ were also quantified in the gold capsules after 15 days of reaction (**Fig. 3**). As expected, neither of these species were detected in the experiments conducted with fluid only (no solid charge). Remarkably, in runs where SL-granite or

441 arfvedsonite were reacted, the presence of fluid did not seem to have an impact on CO₂ and
442 CH₄ production, as both molecules were detected in similar amounts under dry condition
443 (**Fig. 3a, b**). This observation contrasts with the near absence of H₂ released under dry
444 condition (**Fig. 2**). The mineralogical assemblage, i.e., SL-granite or arfvedsonite, also has
445 only a weak impact on CO₂ and CH₄ production (**Fig. 3c, d**). Also expected, a clear effect of
446 pH was observed on gaseous CO₂ production under hydrothermal conditions – from 25 to 35
447 mmol kg_{rock}⁻¹ under acidic condition (0.1 m HCl + 3 m NaCl) to less than 6 mmol kg_{rock}⁻¹
448 under alkaline condition (0.1 m NaOH + 3 m NaCl) – but this result can be easily explained
449 by carbonate speciation and CO₂ solubility as a function of pH. Methane on the other hand,
450 was released in a much lower amount: from 2 to 5 mmol kg_{rock}⁻¹, with no clear fluid,
451 mineralogical or pH effect. This notwithstanding, a discussion on the sources of CO₂ and CH₄
452 is beyond the scope of this study, and these results are provided for information purposes
453 only. We do point out, however, that minerals such as nahcolite and REE (Rare-Earth
454 Elements)-Sr-carbonates have been reported in the hypersolvus granite at Strange Lake and
455 that both CH₄ and CO₂ may be occluded or trapped in melt/fluid inclusions in these minerals
456 (Vasyukova et al., 2016; Vasyukova and Williams-Jones, 2019; Gysi et al., 2013, 2016).

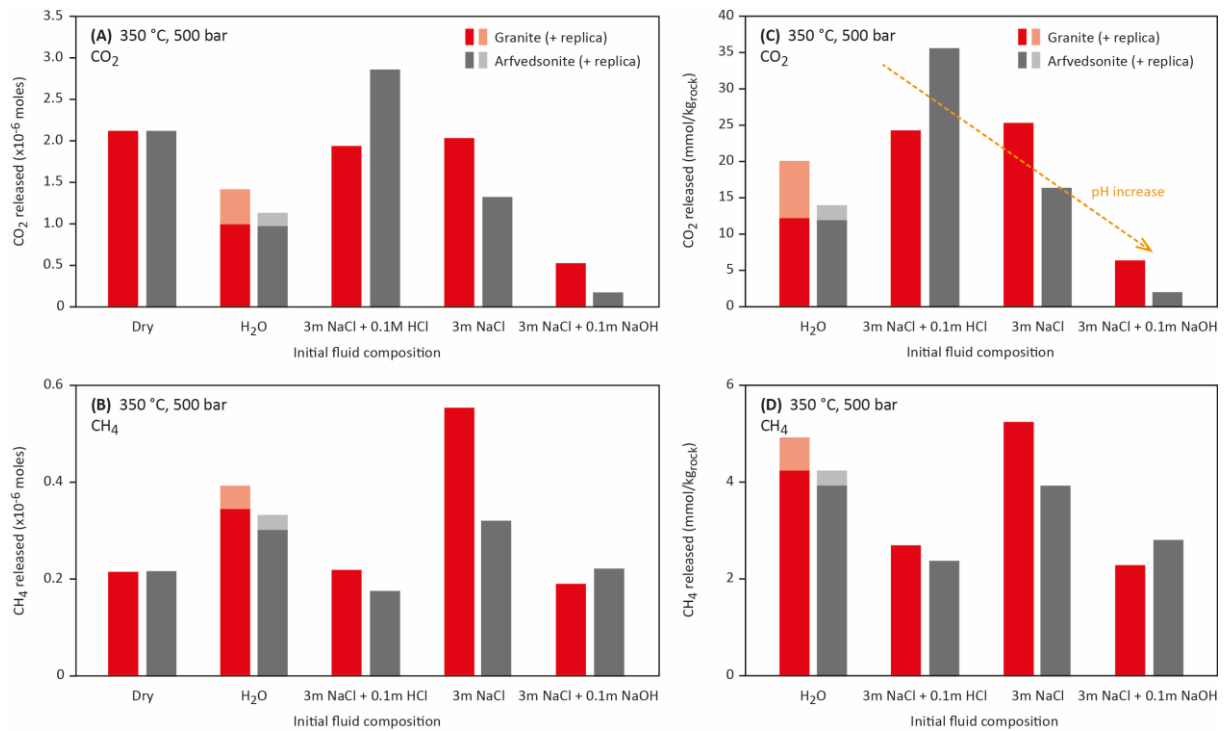


Figure 3. Production of CH₄ and CO₂ after 360 hours elapsed time in gold capsule experiments carried out at 350 °C and 500 bar. (a) and (b) moles of CO₂ and CH₄ produced in the gold capsules as a function of fluid composition, respectively. The annotation “dry” indicates that the gold capsule was loaded with solid material only (no fluid). (c) and (d) show production of CO₂ and CH₄ normalized to the mass of solids (SL-granite or arfvedsonite) as a function of fluid composition, respectively. The orange dashed line depicts a trend of decreasing CO₂ concomitant with increasing pH of the fluid.

3.2 H₂ generation from peralkaline granite alteration at 280 °C and vapor saturation pressure

At 280 °C and vapor saturation pressure, H₂ was produced continually over 650 hours when reacting SL-granite with pure water (**Fig. 4**). After 650 hours had elapsed, H₂ concentration reached 13 mmol kg_{rock}⁻¹. The concentration of CO₂ remained nearly constant at 2 mmol kg_{rock}⁻¹ throughout the run, and traces of CH₄ were detected (below the quantification limit of 10 ppm) at the end of the experiment. Note that the total carbonate concentration is unknown as most of the CO₂ is dissolved in the aqueous phase, given the alkaline pH value recorded on the liquid samples throughout the experiment. The concentrations of major dissolved elements (Si, Al, Na, K, Ca, Mg, Mn, Fe) measured throughout the experiment are provided in the **Supplementary Table S2** and the **Figure S1**. No H₂, CH₄ or CO₂ were

detected when reacting the purified quartz fraction from SL-granite under the same condition (#QTZ280, **Supplementary Table S2**).

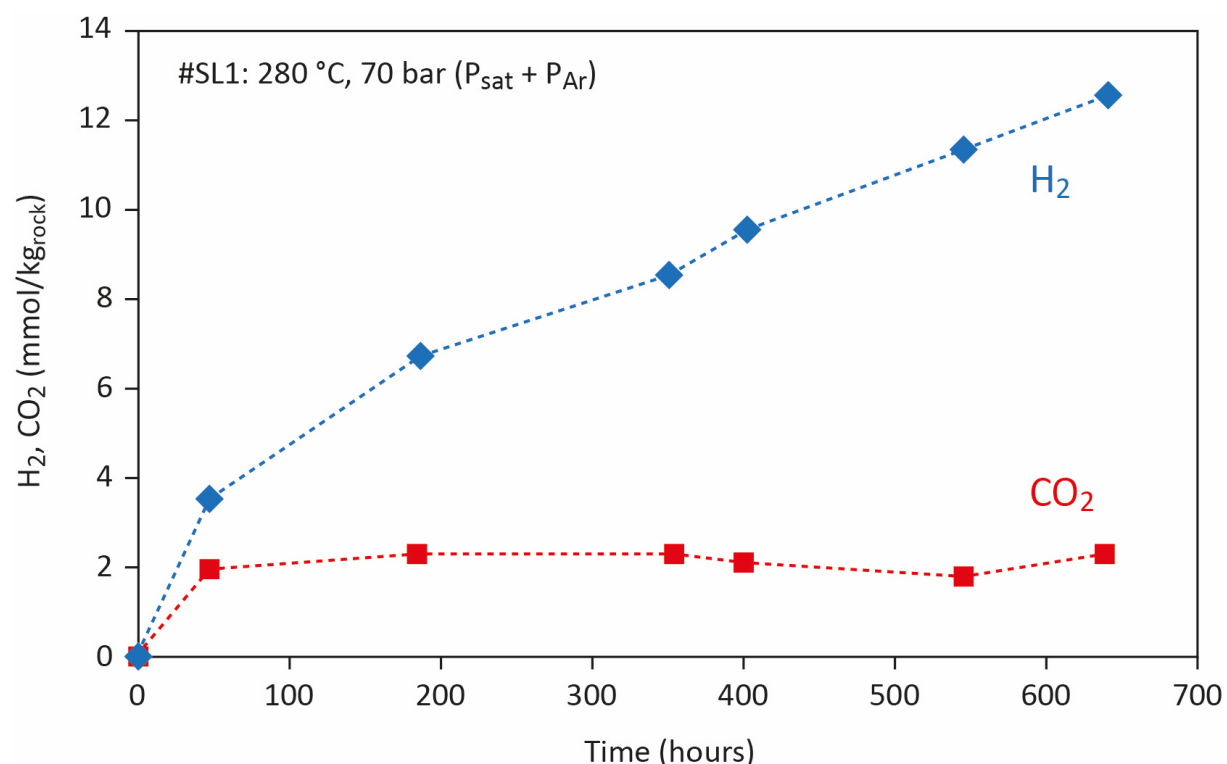


Figure 4. Production of H₂ (blue diamonds) and CO₂ (red squares) as a function of time during experiment #SL1 carried out at 280 °C, 70 bar (P_{sat} + Ar) in the presence of water and SL-granite. Error bars are smaller than the size of the symbols.

3.3 H₂ generation from peralkaline granite alteration up to 400 °C: effect of vapor-brine immiscibility

At 350 °C and 400 bar in a single-phase fluid, H₂ concentration increased rapidly within the first 72 hours of reaction and then followed a relatively constant increase at a slower rate (**Fig. 5**). No significant change in the production rate was observed when temperature was increased from 350 to 400 °C at constant pressure (400 bar). After 552 hours of reaction, NaCl was injected and pressure dropped to 260 bar. Either of these actions alone would have induced phase separation, however, the hydrogen production rate was only

slightly impacted, for a few hours following state change. Despite the fact that a substantial amount of H_2 was generated during the first stage of the experiment, at 350°C and 400 bar, its concentration in the aqueous phase remained well below its solubility threshold, which is ~1.7 m in pure water (Seward and Franck, 1981). Conversely, after phase separation induced by NaCl injection and pressure decrease most of the H_2 was certainly in the vapor phase. Although to this day there is no thermodynamic data to predict the solubility of H_2 in brine nor the vapor/liquid partitioning of H_2 under such condition, it is reasonable to expect the vapor phase to be enriched in H_2 with respect to the liquid phase, due to salting out effect (Bazarkina et al., 2020).

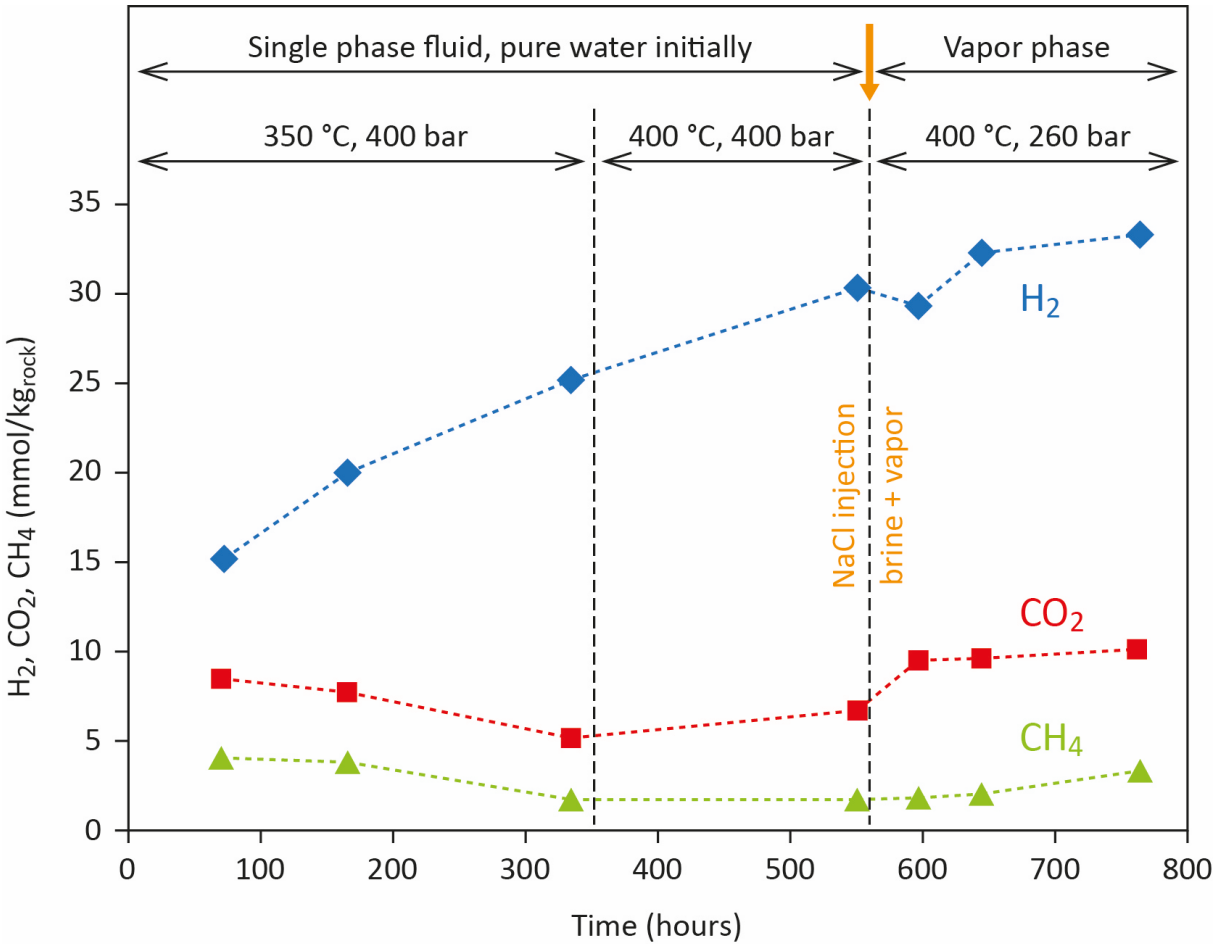


Figure 5. Production of H_2 (blue diamonds), CO_2 (red squares) and CH_4 (green triangles) as a function of time during experiment #SL9 carried out in the presence of water and SL-granite. Temperature, pressure and fluid composition evolve according to 3 consecutive steps as indicated on the figure: 1) 350 °C, 400 bar, pure water initially, then 2) a temperature increase to 400 °C at constant pressure 400 bar, and finally 3) NaCl injection and

pressure decrease to 260 bar at 400 °C. This last step induced phase separation to produce coexisting brine (density = 0.70 g cm⁻¹, 2.7 m NaCl) and vapor (density = 0.19 g cm⁻¹, 0.028 m NaCl). During this stage, sampling was performed from the vapor phase. Error bars are smaller than the size of the symbols.

The concentrations of CO₂ and CH₄ remained relatively constant throughout the experiments, at ~7 and 3 mmol kg_{rock}⁻¹, respectively. Sodium concentrations measured in the vapor phase (~27 mmol kg⁻¹) are in agreement with our thermodynamic predictions (28 mmol kg⁻¹) using the HCh software (Shvarov, 2008). Concentrations of major dissolved elements (Si, Al, Na, K, Ca, Mg, Mn, Fe) measured during the experimental runs are provided in the **Supplementary Table S2** and the **Figure S2**.

3.4 Investigation of solid reaction products

X-Ray diffraction patterns performed on the bulk SL-granite powders, before and after reaction at 280 °C (#SL1) and 400 °C (#SL9) do not provide any clear evidence for the precipitation of secondary minerals (**Supplementary Figure S3a**). After reaction at 280 °C in #SL1 experiment, the most striking feature we observed is extensive dissolution of quartz (**Supplementary Figure S3a**). This observation is consistent with the fact that the reacted solid were cemented in the vessel after this experiment by amorphous silica precipitation. Traces of chlorite (1.8 %), magnetite (0.9 %) and zircon (0.8 %) improved the quantitative analysis (Rietveld refinement) of the XRD pattern collected on solids reacted at 280 °C (#SL1). At 400 °C, magnetite was the only secondary mineral that could be detected by XRD quantitative analysis (0.6 %). However, at such low volumes, identification and quantification of secondary minerals by XRD analysis is challenging. Similarly, no significant mineral neoformation was detected by XRD analysis after reaction of pure arfvedsonite at 350°C, 500 bar in the presence of 3 m NaCl + 0.1 m NaOH (**Supplementary Figure S3b**). However, the X-Ray diffraction patterns collected on the <2 µm fraction recovered after #SL1 and #SL9

experiments confirm the formation of minor chlorite and reveal the presence of other minerals displaying peaks at 11.87, 10.55 and 9.43 °2θ (**Supplementary Figure S3c**), which could be assigned to palygorskite and sepiolite. The presence of a hydrous zirconosilicate tentatively identified as catapleiite was also noticed. Experiments carried out at 350 °C in the presence of SL-granite and 0.1 m NaOH (run #13, Table 1), led to the formation of montmorillonite (**Supplementary Figure S3d**). Aegirine was not detected in the reacted SL-granite samples (bulk and clay fraction).

Regardless, extensive SEM analysis performed on all reacted SL granite powders reveals the presence of clear dissolution features at the surface of arfvedsonite at all temperatures investigated (280, 350, 400 °C) under circumneutral to hyperalkaline condition (**Fig. 6**). The dissolution textures are clearly visible along the edges, corners and cleavages of arfvedsonite crystallites. For runs at 280 °C and 350 °C, the surface of recovered arfvedsonite is partially covered by sub-micrometric (< 200 nm) isolated mounds or lumps of a high-density mineral (bright color under BSE mode). Magnetite, another high-density secondary mineral, was also present in the reaction products from all experiments carried out in the presence of SL-granite + H₂O ± NaOH. Magnetite primarily occurs as small (<1 to ~5 µm) euhedral crystals dispersed throughout the reacted solids or coating on the arfvedsonite surface, in particular after reaction at 400 °C (run #SL9). In addition, tiny precipitates of a fibrous mineral are commonly observed on the edge and cleavages of arfvedsonite, for all temperatures investigated. Phyllosilicates displaying two different textures, fibrous and flaky, are observed either at the surface of arfvedsonite or as isolated aggregates, respectively. Most secondary minerals precipitated at the surface of arfvedsonite during the runs are too small for representative EDX analysis, however, in the case of the platy phyllosilicates aggregates, Fe, Mg, K, Na and Al were clearly detected. The presence of chlorite would reconcile this texture with the chemical analyses and the interpretation of the XRD patterns.

When arfvedsonite was reacted alone (350 °C and 500 bar) in pure water or under hyperalkaline conditions, the dissolution features were far less pronounced and no secondary phases were detected at its surface, by SEM observation. Also, no signs of alteration were observed on arfvedsonite in runs done under acidic condition, independently of whether it was alone or embedded within SL-granite.

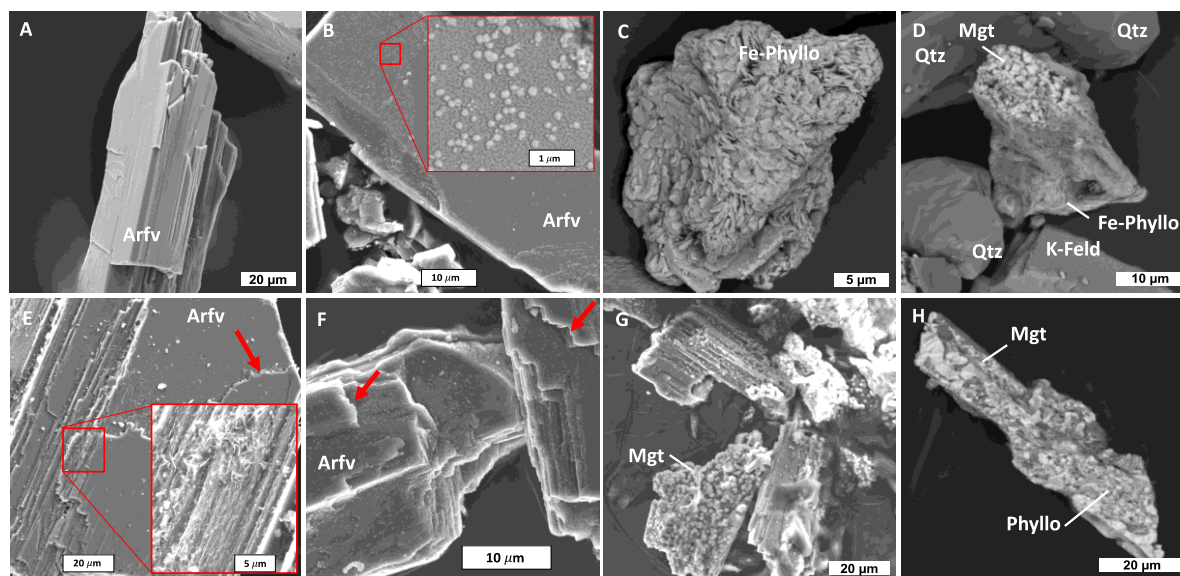


Figure 6. Backscattered electron (BSE) and secondary electron (SE) images of unreacted arfvedsonite and representative reaction products after hydrothermal alteration of SL-granite at 280, 350 and 400 °C. (a) BSE image of unreacted arfvedsonite (Arfv). (b) BSE image of arfvedsonite after reaction at 280 °C (run #SL1) with tiny isolated zircon lumps (<200 nm) on its surface (inset). (c) BSE image of Fe-rich phyllosilicate (Fe-Phyllo) observed in the bulk solids after hydrothermal alteration of SL-granite at 280 °C (run #SL1). (d) BSE images of magnetite (Mgt) crystals imbedded in mats of platy Fe-phyllosilicate after reaction at 280 °C (run #SL1). Quartz (Qtz) and K-feldspar (K-Feld) crystals from SL-granite are also visible. (e) and (f) SE images of arfvedsonite after hydrothermal alteration of SL-granite at 350 °C in the presence of water. The surface of arfvedsonite displays clear dissolution features on the edges, corners and cleavage surfaces (red arrows). The inset in (e) shows the presence of tiny fibrous precipitates along the arfvedsonite cleavages. The surface of arfvedsonite in (f) is also covered with tiny zircon lumps. (g) BSE image of arfvedsonite crystals nearly fully coated by interbedded octahedral magnetite (Mgt) crystals after reaction at 400 °C (run #SL9). (h) BSE image of arfvedsonite crystals fully coated by magnetite and phyllosilicates after reaction at 400 °C (run #SL9).

TEM-EDX observations and analysis performed on FIB ultrathin sections milled perpendicularly to the arfvedsonite surface reacted at 280 °C (#SL1) and 350 °C, initially in the presence of granite and pure water, reveal without any ambiguity that the sub-micrometric

isolated lumps detected by SEM imaging are ZrSiO_4 nodules precipitated at its surface (**Fig. 7**). These nodules consist of polycrystalline zircons, with radial growth, constituting half-spheres whose radius does not exceed 200 nm (**Fig. 7d**). They sit on the surface of the arfvedsonite crystallites without crystal connection to them, indicated by the extremely clean and sharp interface between zircon and arfvedsonite (**Fig. 7e, f**). In the same way, zircon nodules seem to precipitate preferentially on large flat and clean arfvedsonite surfaces, rather than in dissolution pits. TEM observations on FIB sections also reveal that monocrystalline arfvedsonite, apart from dissolution areas (edges, corners and cleavages), is not altered, even at the nanoscale, where zircon precipitated (**Fig. 7f**).

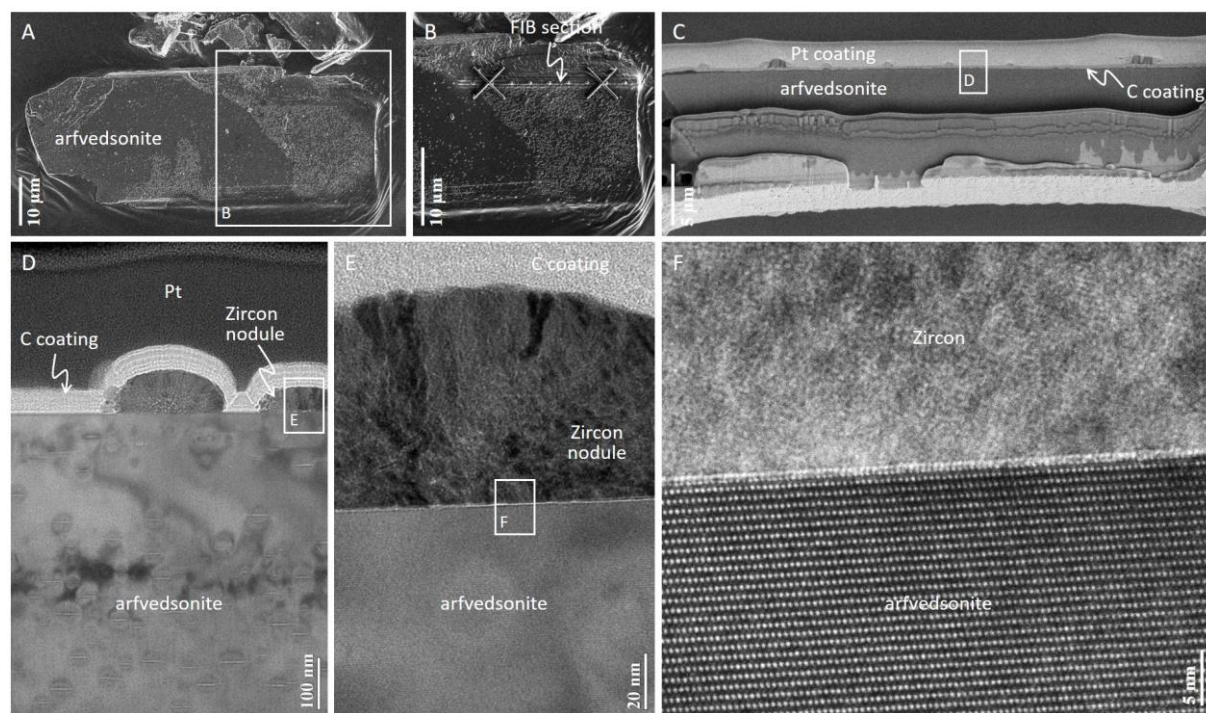


Figure 7. SEM and TEM images of arfvedsonite-zircon nodule interface. (a) SEM image of carbon-coated arfvedsonite crystal covered with nanometric nodules. (b) SEM image of the crystal area targeted for FIB foil cutting. The emplacement of the FIB foil is identified by a platinum deposit (in the shape of a cross and dots). (c) FIB foil extracted from the section defined in (b), with a continuous platinum strap on top of it. The FIB foil presents different cutting thicknesses, the arfvedsonite-zircon nodule interface being the thinnest area. Carbon coating is also visible. (d) Bright-field TEM image of the FIB foil from (c) showing radial-growth of zircon nodules placed on the clean surface of the arfvedsonite crystal. Platinum strap (Pt) and carbon coating are indicated. (e) Expanded view from image (d) presenting a polycrystalline zircon nodule in contact with arfvedsonite. (f) High-resolution TEM image of the interface, showing the crystalline structure of the two phases, with no inter-crystalline connection.

607
608
609
610
611
612
613
614
615
616
617
618
619
620
621

The iron redox state of three arfvedsonite samples – unreacted arfvedsonite and reacted arfvedsonite at 280 °C and at 400 °C (respectively runs #SL1 and #SL9) – was studied by STXM-XANES. The **Figure 8** compares rescaled representative spectra from each sample, corrected for background. Fe L_{2,3}-edge spectra display four major peaks, two for the L₃-edge are noted L₃-a (~708.7 eV) and L₃-b (~710.2 eV), two for the L₂-edge are noted L₂-a (~720 eV) and L₂-b (~723.5 eV). L₃-a and L₂-a peaks are mainly affected by the Fe²⁺ content, while the L₃-b and L₂-b peaks are affected by the Fe³⁺ content. Here, unreacted arfvedsonite and #SL1 spectra have a similar shape, i.e. a high L₃-a peak and a small L₃-b peak indicating ferrous phases, while #SL9 spectrum shows an inverted intensity ratio, typical of ferric phases (**Fig. 8**). The estimation of Fe³⁺/Fe_{total} ratio is based on the L₃-b/L₃-a peak intensity ratio as proposed by Bourdelle et al. (2013), and indicates 33 %, 38 % and 79 % of ferric iron in unreacted, reacted #SL1 and reacted #SL9 arfvedsonite, respectively. These estimates are based on 4 to 6 spectra per samples, showing intrasample homogeneity.

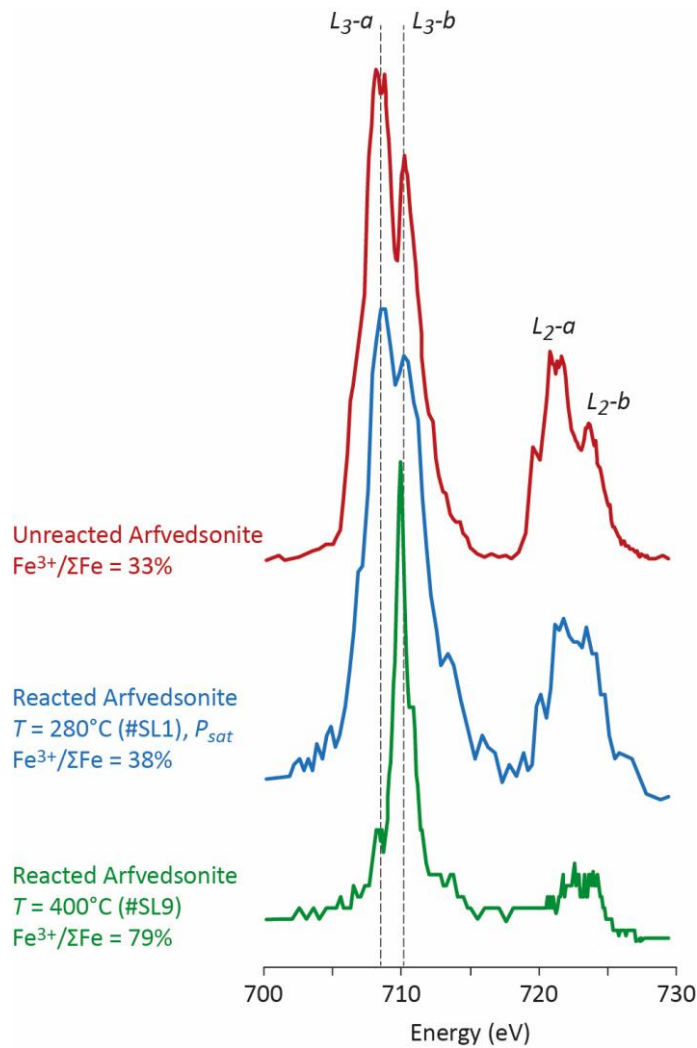


Figure 8. Representative XANES spectra at the Fe $L_{2,3}$ -edges for unreacted (in red) and reacted (#SL1 in blue, #SL9 in green) arfvedsonites. Spectra have been normalized to the integral Fe L_3 -edge intensity, and shifted vertically for clarity (normalised intensity with arbitrary unit). The vertical dashed lines represent the energies fixed to determine the $\text{Fe}^{3+}/\text{Fe}_{\text{total}}$ ratio from the intensities of L_3 -peaks, according to the procedure of Bourdelle et al. (2013).

4. Discussion

4.1 Source of H_2

From the experimental results detailed in the preceding sections, we learned that hydrogen generation in the presence of SL-granite or arfvedsonite occurs under near-neutral to alkaline hydrothermal condition, at $T \geq 280^\circ\text{C}$. A range of blank experiments assessed that no H_2 was produced from the experimental apparatus and that the release of the H_2 occluded

in minerals or entrapped in quartz-hosted fluid inclusions from SL-granite was negligible (< 5 %). Thus, we can be confident that H₂ in our experiments was indeed produced during water-rock interaction.

Production of H₂ occurred when arfvedsonite was the only mineral introduced in the hydrothermal system. Even higher amounts of H₂ were generated when SL-granite (containing 10 wt% arfv) was reacted (**Fig. 2**). The role of granite could either imply that H₂ is supplied by more than one source, or that arfvedsonite alteration is enhanced in the presence of other minerals. The presence of Fe is reported in alkali feldspar from the hypersolvus granite, however, it consists of small amounts of ferric iron (0.23 wt% Fe₂O₃, or about 0.01 apfu Fe³⁺ - Siegel et al., 2018), which cannot oxidize to produce H₂. On the other hand, the second hypothesis is more plausible, given that hydrothermal alteration of granite naturally leads to alkaline conditions that, as seen above, favor the H₂-producing reaction. In addition, altering a rock instead of only a mineral will release a range of elements into solution that are likely to enhance precipitation of additional secondary minerals, in particular phyllosilicates. This is consistent with the presence of higher amounts of secondary minerals such as magnetite and phyllosilicates when the granite, instead of arfvedsonite alone, was included in the experimental runs.

Experimental replicates performed at 350 °C in gold capsules, using pure water as starting solution, showed a 10 to 30 % difference in the amount of H₂ produced, when comparing two runs carried out under the same conditions. Nevertheless, despite these significant uncertainties on the amount of H₂ produced, a constant result was that alkaline conditions promoted H₂ generation and that salinity of the reacting fluid had a slightly negative impact on H₂ production (**Fig. 2b**). Similar conclusions were drawn recently from laboratory experiments of olivine serpentinization at 200–280 °C (Lamadrid et al., 2017; McCollom et al., 2020b).

661

662 4.2. Reaction mechanism

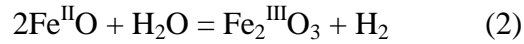
663 Another question that needs addressing concerns the reaction mechanism of H₂
664 production. On the basis of petrographic observations, it has been proposed that arfvedsonite
665 is replaced by aegirine under hydrothermal condition at $T \geq 350$ °C, and that this replacement
666 releases H₂, according to the **Equation 1** (Salvi and Williams-Jones, 1997; Potter et al.,
667 2013). Replacement of arfvedsonite by aegirine is a common feature of peralkaline rocks
668 (e.g., Marks and Markl, 2017; Bernard et al., 2020), and a beautiful example of arfvedsonite
669 alteration into aegirine is shown in **Figure 1**. In the laboratory, aegirine has been synthesized
670 at temperatures as low as 200 °C in aqueous solutions; below this temperature Na– Fe-
671 phyllosilicates form instead (Decarreau et al., 2004). In our study, however, aegirine
672 formation was not detected, at any of the conditions tested. Possible reasons may include the
673 relatively low pressure (≤ 400 bar) and short duration (< 30 days) of our experiments.
674 Nonetheless, two important lines of evidence demonstrate the occurrence of arfvedsonite
675 oxidative dissolution. Firstly, when observed under an electron microscope, the arfvedsonite
676 surface clearly displays typical features of dissolution, such as dissolved edges and corners as
677 shown in **Figure 6f**. In addition, reacted arfvedsonite is covered by an unexpected multitude
678 of tiny distinct zircon lumps, particularly visible in the experiment carried out at 280 °C and
679 350 °C in the presence of SL-granite + H₂O (**Fig. 6b, e and f**). In SL-granite, zirconium is
680 present in the form of zircon crystals, but also occurs in the structure of arfvedsonite (EMPA
681 analysis indicate ~1200 ppm). Contrarily to arfvedsonite, primary zircon grains do not show
682 any sign of dissolution. This, together with the fact that the secondary zircon lumps occur
683 only at the surface of arfvedsonite, suggests that Zr was supplied by dissolution of the latter.
684 Because of its extremely low solubility, zircon precipitated at the surface of its source, rather
685 rapidly as suggested by the apparent botryoidal habit of these lumps (**Fig. 7**). A second line of

evidence for oxidative dissolution of arfvedsonite is the presence of several Fe^{III}-bearing alteration minerals in the reacted experimental powders. Magnetite was identified on the surface of arfvedsonite and disseminated in the bulk powder, at all investigated temperatures and in the presence of SL-granite + H₂O ± NaOH (**Fig. 6d, g and h**). Phyllosilicates were also detected, their presence confirmed by XRD and SEM analysis (**Fig. 6c, d, e and h**), and display either fibrous or flaky textures (**Fig. 6c and e**). Possibly, chlorite and Na-montmorillonite may also be present, according to some features of the XRD and EDX patterns recorded from SL-Granite reacted at 280 °C. Finally, STXM-XANES analysis revealed a clear increase of the Fe³⁺/Fe_{total} ratio of the arfvedsonite after reaction at 280 °C and 400 °C (**Fig. 8**). Because the STXM-XANES probes particles through their thickness, only very thin fragments of arfvedsonite – transparent to X-ray (thickness < 100 nm) – were targeted, i.e. probably the most altered crystallites. Therefore, Fe³⁺/Fe_{total} values (**Fig. 8**) could be considered either as resulting from structural oxidation of Fe^{II} into Fe^{III}, more detectable in very thin particles, or as an average between a preserved crystal core and an altered ultrathin external layer at the grain surface. The relationship between iron redox estimates and experiment conditions (increasing Fe³⁺ proportions with increasing run temperature) can therefore testify of an ongoing process of arfvedsonite oxidation. This observation may also provide a hint for the absence of aegirine, whose precipitation would supposedly occur at a higher oxidative level, not yet attained during the experiments.

4.3 Alteration progress

Assuming that H₂ is entirely produced by arfvedsonite dissolution through oxidation of structural Fe^{II} into Fe^{III}, one can calculate the extent of alteration progress. Given i) the molar mass of arfvedsonite (~960 g mol⁻¹), ii) the Fe^{II} stoichiometry in arfvedsonite (3.07 mole Fe(II) per mole of arfvedsonite), and iii) the mass balanced H₂ production from Fe^{II}

oxidation into Fe^{III} (the generalized reaction can be represented according to the **Equation 2**), we estimate that 1 kg of arfvedsonite can produce a maximum of 1.54 moles of H₂ if all the Fe^{II} is oxidized into Fe^{III}.



Note that using the **Equation 1** to calculate the H₂ production from arfvedsonite oxidation leads to a similar result: 1.74 moles of H₂ produced per kg of arfvedsonite reacted. For comparison, McCollom et al. (2016) show that complete serpentinization of 1 kg San Carlos olivine produces up to 0.3 moles of H₂ at 265–300 °C. Thus, arfvedsonite alteration can produce ~5 times more H₂ than olivine serpentinization, per mass unit of mineral reacted. Similarly, the H₂ production from SL-Granite and peridotite can also be compared. The latter can produce about 0.37 moles of H₂ per kg of rock altered, assuming an FeO content of 8 wt% and that 66% of the iron gets oxidized during serpentinization (Klein et al., 2014). Because arfvedsonite represents only 10 wt% of SL-granite, the H₂ potential of this rock is 0.17 moles per kg, which is about two times less than that of peridotite.

Using these mass balance calculations, together with the known amounts of H₂ produced during the experiments, allows estimating the minimum amount of arfvedsonite reacted. It turns out that at least 23 wt% of arfvedsonite were dissolved in the experiment where SL-granite was reacted at 350–400 °C, in an initial pure water medium. Similarly, ~8 wt% arfvedsonite was dissolved during run #SL1 where SL-granite was reacted at 280 °C in the presence of pure water. Given the proportions of arfvedsonite in SL-granite (10 wt%), these maximum estimates are in line with SEM and XRD observations made on the reacted solid reaction products. In the case of experiments conducted with pure arfvedsonite at 350 °C with either pure water, or water + 3 m NaCl + 0.1 m NaOH, our estimate implies that ~10 wt% arfvedsonite would have reacted. This value contrasts with the rather weak dissolution/precipitation features observed at the surface of arfvedsonite after these two

experiments, and the non-detection of secondary by-products by XRD analysis. To account for the latter, one explanation may lie in the low water-to-rock mass ratio ($W/R = 1$) in these experiments. Another possibility is that secondary phases were lost during the opening of the gold capsule, as its strong deformation and the low mass of reacted material render this operation quite complex. More experiments using longer reaction time and higher amounts of sample will help shedding more light on the mechanism of arfvedsonite alteration.

4.4. Rate of H_2 generation and comparison with serpentinization

Hydrogen production recorded as a function of time during our hydrothermal experiment carried out at 280 °C (#SL1) and 350 °C in the presence of a sieved fraction of SL-granite (53 – 212 μm) can be compared with experiments carried out at 300 °C on harzburgite and San Carlos olivine powder of similar grain size by Grozeva et al. (2017) and McCollom et al. (2016), respectively (**Fig. 9**). The water/rock ratio is the main significant parameter that differs from these experiments. Hydrogen concentration data from Grozeva et al. (2017) have been recomputed to be plotted in the same unit as the other experiments (i.e mmol of H_2 per kg of rock – see **Supplementary Table S3**). Hydrogen generation rates from SL-granite and harzburgite alteration are similar, at least during the early stage of reaction. After 500 hours of reaction time, the total amount of H_2 generated during run #SL1 was 1.5 times greater than that obtained with San Carlos olivine.

In our run, after 48 hours at 280 °C, H_2 was generated at a relatively constant rate of $1.47 \times 10^{-5} \text{ mol kg}_{\text{rock}}^{-1} \text{ h}^{-1}$. Assuming that all H_2 is produced from arfvedsonite alteration (10 wt% of granite), and given the specific surface area of this amphibole ($0.30 \text{ m}^2 \text{ g}^{-1}$), we obtain a rate of H_2 production of about $1100 \text{ pmol cm}^{-2} \text{ day}^{-1}$. This value lies within the range of H_2 production rate reported for olivine serpentinization by McCollom et al. (2016) at 300 °C: 100 – 2000 $\text{pmol cm}^{-2} \text{ day}^{-1}$. The rate of hydrogen production derived from the experiment carried

out at 350 – 400 °C and 400 bar (#SL9) is about 2 times higher than at 280 °C: 3.0×10^{-5} mol $\text{kg}_{\text{rock}}^{-1} \text{h}^{-1}$ or $2200 \text{ pmol.cm}^{-2}.\text{day}^{-1}$. The absence of coating or passivation observed at the surface of the arfvedsonite clearly plays in favor of a high rate of alteration, as no diffusion process of the reactants through secondary phases is there to slow the reaction down. During olivine serpentinization, hydrogen production rate peaks at about 300 °C and then decreases abruptly as temperature increases. This is because olivine, being part of the equilibrium mineral assemblage, limits the amount of Fe(II) available for H_2 generation (McCollom et al., 2016). Currently, the temperature dependence of H_2 production rate during arfvedsonite alteration is poorly constrained, but the trend observed for olivine serpentinization does not seem to be valid for peralkaline granite.

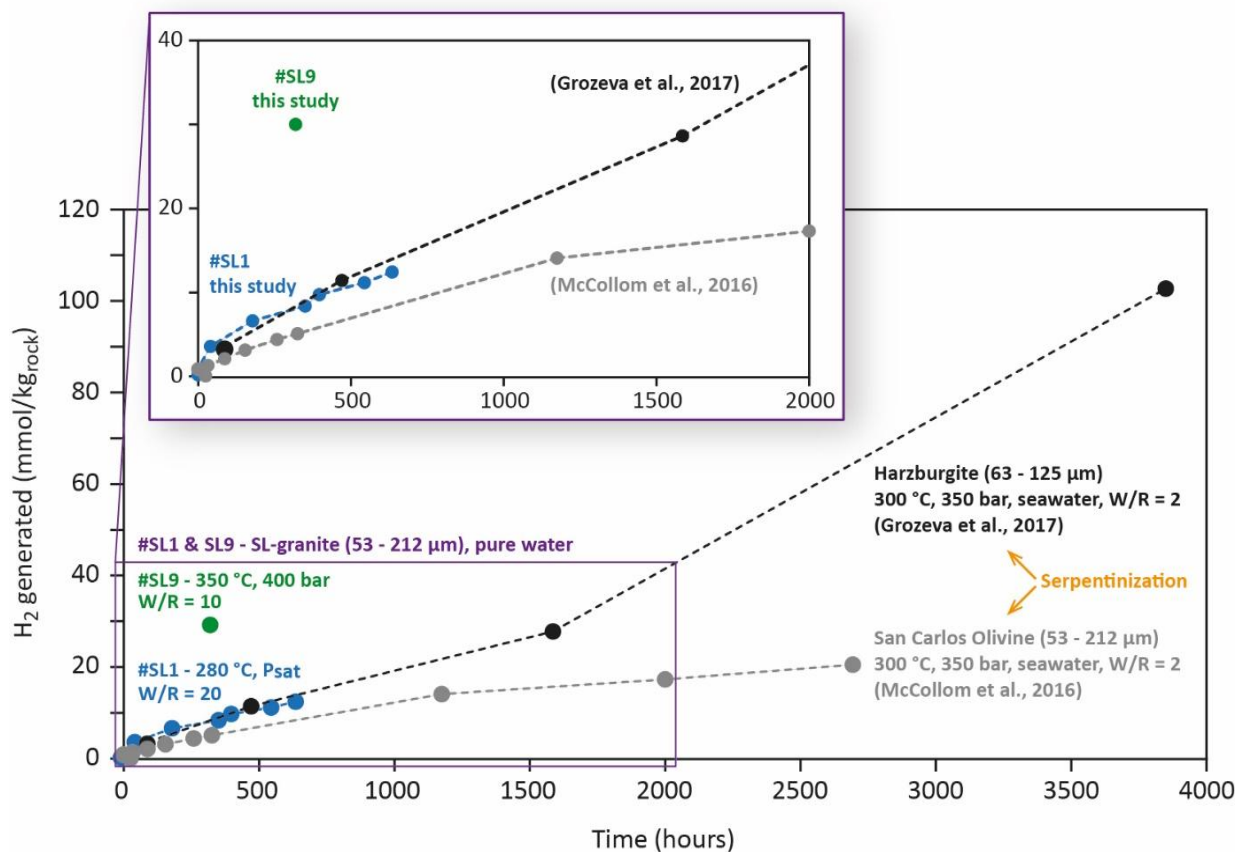


Figure 9. Comparison of H_2 generation during San Carlos olivine (grey dots), and harzburgite (black dots) serpentinization at 300 °C, with SL granite hydrothermal alteration at 280 °C (red dots) and 350 °C (green dot). The inset graph is a zoom on the first 2000 hours of reaction.

776

777 However, it seems clear that the presence of the minerals forming the granite has a
778 strong impact on the H₂ production rate, as mentioned previously. In particular, albite and
779 microcline are an important source of aluminum, an element that plays a key role in the
780 precipitation of phyllosilicates. As already observed for serpentinization (Andreani et al.,
781 2013), presence of aluminum may increase both the solubility and dissolution rate of
782 arfvedsonite, by enhancing the precipitation of phyllosilicates such as chlorite and
783 montmorillonite.

784

785 4.5 Implications for H₂ production and exploration in peralkaline rocks

786 If there is a consensus in the scientific community on the abiotic origin of hydrogen,
787 methane, and associated higher-order hydrocarbons found in agpaitic peralkaline igneous
788 intrusions, the source of these gases is still subject of debate in the literature (e.g., Marks and
789 Markl, 2017). Some authors consider that CH₄ plus minor to moderate amounts of H₂ exsolve
790 from the magma at 450–500 °C, together with an immiscible aqueous fluid of high salinity
791 (25 wt% NaCl eq.) (Konnerup-Madsen et al., 1985; Beeskow et al., 2006; Krumrei et al.
792 2007; Vasyukova et al., 2016, 2019). Other workers propose that the hydrocarbons formed by
793 late to post-magmatic Fischer-Tropsch-like synthesis, with the H₂ needed to drive this
794 reaction being produced from alteration of primary igneous minerals such as arfvedsonite
795 (Salvi and Williams-Jones, 1997, Potter et al., 2004; 2013). Production of some H₂ by
796 polymerization of primary hydrocarbons has also been proposed (Krumrei et al. 2007).

797 At Strange Lake, early CH₄-rich inclusions may contain up to 97 mol% CH₄ and 3
798 mol% H₂ (Salvi and Williams-Jones, 1992, 1997, 2006; Vasyukova et al., 2016). From the
799 spatial distribution of fluid and melt inclusions, Vasyukova et al. (2016) inferred that the fluid
800 carrying these reduced gases coexisted with a pegmatite melt at the time of entrapment and

concluded that it had exsolved from the melt. However, the fate of H₂ remains unclear, as this molecule was also measured in secondary fluid inclusions by the same authors. Also, most of the fluid inclusion data collected so far at Strange Lake rely on bulk gas analysis (Salvi and Williams-Jones, 1997; Vasyukova et al., 2016), and the few in-situ Raman measurements available (Vasyukova et al., 2016) were not designed to specifically target H₂ – as these authors point out, its strongest vibration at 4156 cm⁻¹ is beyond the wavenumbers range accessible with the spectrometer used. On the other hand, Potter et al. (2004) were able to measure up to 40 mol% H₂ at 400 bar in CH₄-dominant fluid inclusions from the Lovozero pluton (Kola Peninsula, Russia), using a mass spectrometer coupled to an on-line GC-crusher system (see also Salvi and Williams-Jones, 2003). Based on detailed fluid inclusion petrography, in situ Raman spectroscopy and textural relationships, Potter and coworkers concluded that these inclusions were trapped during post-magmatic hydrothermal alteration of an early mineral assemblage. The rarity of H₂O-dominant inclusions in the Lovozero samples and the coexistence of these inclusions in the same trails as the CH₄-dominant inclusions implies coeval, immiscible trapping of the aqueous and the carbonic fluids, at or below the CH₄ - H₂O solvus at ~350 °C, leaning towards a post-magmatic origin. This is also supported by the microthermometric data for the H₂O-dominant inclusions, which homogenize to vapor between 290 and 350 °C.

The data presented here do not resolve this debate, but they clearly demonstrate that H₂ can be produced by water-rock interaction, i.e., during the post-magmatic stage, via the alteration of arfvedsonite to aegirine, a widespread process in peralkaline rocks, particularly the agpaitic variety (e.g., Bernard et al., 2020). Given the depth of these plutons (maximum of 12.5 km for the Khibiny and Lovozero system; Arzamastsev et al., 2000, 2013), it is possible that, in some cases, temperatures of ca. 200 °C or above may sustain active hydrothermal activity that could produce alteration of these rocks at depth, thereby triggering H₂ generation,

nowadays. Agpaitic peralkaline igneous intrusion may thus represent fertile geological setting for H₂ exploration for energy production purposes.

5. Conclusion

The results of this study clearly show that H₂ can be produced via the hydrothermal alteration of arfvedsonite at $T \geq 280$ °C in agpaitic peralkaline igneous intrusions. Oxidation of structural Fe^{II} into Fe^{III} with concomitant reduction of water explains well this observation. After experimental reaction, arfvedsonite exhibits obvious dissolution feature at its surface, and magnetite, phyllosilicates and secondary zircons become present. Circumneutral to alkaline conditions clearly promote H₂ generation as it is the case for serpentinization. Hydrogen generation is also enhanced when reacting granite instead of only arfvedsonite. Aluminum, from alkali feldspar dissolution, may increase the solubility of arfvedsonite through the precipitation of phyllosilicates. In terms of rate, H₂ generation from arfvedsonite alteration in the presence of granite is a more efficient process than serpentinization of olivine or harzburgite.

Aegirine, a very common product of arfvedsonite alteration in these granites, was not observed in this study. The effect of pressure, oxygen fugacity, and length of reaction time remains to be evaluated to better constrain the reaction kinetics. Vasyukova et al. (2016) propose that the cooling of Strange Lake pluton was isobaric and, based on the intersection of isochores for carbonic and aqueous fluid inclusions, took place at a pressure of ~1100 bar. They also note that late alteration of arfvedsonite may continue at temperature as low as 150 °C, with hematite and Fe-celadonite as secondary alteration phases (Vasyukova and Williams-Jones, 2019). Thus, alteration of arfvedsonite and SL-granite at lower temperature would also deserve further investigations.

850

851 **Acknowledgments**

852 This study was financially supported by CNRS -INSU (project CESSUR) and the French
853 National Research Agency ANR through the H2Kola project (AAPG 2020 – CE01 –
854 H2KOLA). Laurent Truche acknowledges support from the Institut Universitaire de France.
855 Gilles Bessaque is warmly thanked for his constant help while handling the Coretest
856 autoclave and fixing numerous leakage and seizing issues. EPMA and XRD analysis were
857 carried out at ISTerre by Valentina Batanova and Nathaniel Findling, respectively. We are
858 most grateful to the PSI SLS synchrotron, especially Benjamin Watts (PolLux beamline) for
859 technical advice, and to the SOLEIL synchrotron, especially Rachid Belkhou for user support.
860 Thanks are also extended to David Troadec and IEMN (Cité Scientifique, av. Poincaré CS
861 60069, 59652 Villeneuve d’Ascq Cedex). The TEM national facility at Institut Chevreul
862 (Lille, France) is supported by the Conseil Régional du Nord-Pas de Calais, the European
863 Regional Development Fund (ERDF), and the Institut National des Sciences de l’Univers
864 (INSU, CNRS).

865

866 **Figure captions**

867

868 **Figure 1.** Geological map of the Strange Lake pluton (courtesy of O. Vasyukova) locating the
869 sample of hypersolvus granite used for the experiments (left-hand side). On the right-hand
870 side is shown a sample of altered pegmatite where the replacement of arfvedsonite (large dark
871 green crystals) by aegirine (light green) is clearly visible. The fluid inclusions displayed in the
872 inset represent an example of coexisting L- and V-rich populations, where the latter inclusions

contain hydrogen as well as higher-order hydrocarbons, showing fluorescence under UV illumination. qtz = quartz, fds = feldspars, arf = arfvedsonite, aeg = aegirine.

Figure 2. Production of H_2 after 360 hours elapsed time in the gold capsule experiments carried out at 350 °C and 500 bar. Different initial fluid compositions were tested to evaluate the effect of pH and salinity. (a) Experiments carried out in the presence of SL-granite (red) or arfvedsonite (black) are compared to the blanks: fluid only (dashed lines) or quartz + 3 m NaCl (grey star). The notation “dry” indicates that the gold capsule was loaded with solid material only (no fluid). The 2 replicates performed in the presence of water + SL-granite or arfvedsonite are shown in light red and light grey, respectively. (b) Production of H_2 normalized to the mass of solids (SL-granite or arfvedsonite) as a function of fluid composition. Error bars reflect the cumulative uncertainty associated with measuring the volume of gas released after piercing the gold capsules and with the analytical uncertainty.

Figure 3. Production of CH_4 and CO_2 after 360 hours elapsed time in gold capsule experiments carried out at 350 °C and 500 bar. (a) and (b) moles of CO_2 and CH_4 produced in the gold capsules as a function of fluid composition, respectively. The annotation “dry” indicates that the gold capsule was loaded with solid material only (no fluid). (c) and (d) show production of CO_2 and CH_4 normalized to the mass of solids (SL-granite or arfvedsonite) as a function of fluid composition, respectively. The orange dashed line depicts a trend of decreasing CO_2 concomitant with increasing pH of the fluid.

Figure 4. Production of H_2 (blue diamonds) and CO_2 (red squares) as a function of time during experiment #SL1 carried out at 280 °C, 70 bar ($P_{sat} + Ar$) in the presence of water and SL-granite. Error bars are smaller than the size of the symbols.

898

899 **Figure 5.** Production of H₂ (blue diamonds), CO₂ (red squares) and CH₄ (green triangles) as a
900 function of time during experiment #SL9 carried out in the presence of water and SL-granite.
901 Temperature, pressure and fluid composition evolve according to 3 consecutive steps as
902 indicated on the figure: 1) 350 °C, 400 bar, pure water initially, then 2) a temperature increase
903 to 400 °C at constant pressure 400 bar, and finally 3) NaCl injection and pressure decrease to
904 260 bar at 400 °C. This last step induced phase separation to produce coexisting brine
905 (density = 0.70 g cm⁻¹, 2.7 m NaCl) and vapor (density = 0.19 g cm⁻¹, 0.028 m NaCl). During
906 this stage, sampling was performed from the vapor phase. Error bars are smaller than the size
907 of the symbols.

908

909 **Figure 6.** Back-scattered electron (BSE) and secondary electron (SE) images of unreacted
910 arfvedsonite and representative reaction products after hydrothermal alteration of SL-granite
911 at 280, 350 and 400 °C. (a) BSE image of unreacted arfvedsonite (Arfv). (b) BSE image of
912 arfvedsonite after reaction at 280 °C (run #SL1) with tiny isolated zircon lumps (<200 nm) on
913 its surface (inset). (c) BSE image of Fe-rich phyllosilicate (Fe-Phyllo) observed in the bulk
914 solids after hydrothermal alteration of SL-granite at 280 °C (run #SL1). (d) BSE images of
915 magnetite (Mgt) crystals imbedded in mats of platy Fe-phyllosilicate after reaction at 280 °C
916 (run #SL1). Quartz (Qtz) and K-feldspar (K-Feld) crystals from SL-granite are also visible.
917 (e) and (f) SE images of arfvedsonite after hydrothermal alteration of SL-granite at 350 °C in
918 the presence of water. The surface of arfvedsonite displays clear dissolution features on the
919 edges, corners and cleavage surfaces (red arrows). The inset in (e) shows the presence of tiny
920 fibrous precipitates along the arfvedsonite cleavages. The surface of arfvedsonite in (f) is also
921 covered with tiny isolated zircon lumps. (g) BSE image of arfvedsonite crystals nearly fully
922 coated by octahedral interbedded magnetite (Mgt) crystals after reaction at 400 °C (run

#SL9). (h) BSE image of arfvedsonite crystals fully coated by magnetite and phyllosilicates after reaction at 400 °C (run #SL9).

Figure 7. SEM and TEM images of arfvedsonite-zircon nodule interface. (a) SEM image of carbon-coated arfvedsonite crystal covered with nanometric nodules. (b) SEM image of the crystal area targeted for FIB foil cutting. The emplacement of the FIB foil is identified by a platinum deposit (in the shape of a cross and dots). (c) FIB foil extracted from the section defined in (b), with a continuous platinum strap on top of it. The FIB foil presents different cutting thicknesses, the arfvedsonite-zircon nodule interface being the thinnest area. Carbon coating is also visible. (d) Bright-field TEM image of the FIB foil from (c) showing radial-growth of zircon nodules placed on the clean surface of the arfvedsonite crystal. Platinum strap (Pt) and carbon coating are indicated. (e) Expanded view from image (d) presenting a polycrystalline zircon nodule in contact with arfvedsonite. (f) High-resolution TEM image of the interface, showing the crystalline structure of the two phases, with no inter-crystalline connection.

Figure 8. Representative XANES spectra at the Fe L_{2,3}-edges for unreacted (in red) and reacted (#SL1 in blue, #SL9 in green) arfvedsonites. Spectra have been normalized to the integral Fe L₃-edge intensity, and shifted vertically for clarity (normalised intensity with arbitrary unit). The vertical dashed lines represent the energies fixed to determine the Fe³⁺/Fe_{total} ratio from the intensities of L₃-peaks, according to the procedure of Bourdelle et al. (2013).

Figure 9. Comparison of H₂ generation during San Carlos olivine (grey dots), and harzburgite (black dots) serpentinization at 300 °C, with SL granite hydrothermal alteration at 280 °C (red dots) and 350 °C (green dot). The inset graph is a zoom on the first 2000 hours of reaction.

References

- Arzamastsev, A.A., Glaznev, V.N., Raevsky, A.B. and Arzamastseva, L.V., 2000. Morphology and internal structure of the Kola Alkaline intrusions, NE Fennoscandian Shield: 3D density modelling and geological implications. *Journal of Asian Earth Sciences*, 18(2), pp.213-228.
- Arzamastsev, A.A., Arzamastseva, L.V., Zhirova, A.M. and Glaznev, V.N., 2013. Model of formation of the Khibiny-Lovozero ore-bearing volcanic-plutonic complex. *Geology of Ore Deposits*, 55(5), pp.341-356.
- Andreani, M., Daniel, I. and Pollet-Villard, M., 2013. Aluminum speeds up the hydrothermal alteration of olivine. *American Mineralogist*, 98(10), pp.1738-1744.
- Bazarkina, E.F., Chou, I.M., Goncharov, A.F. and Akinfiev, N.N., 2020. The Behavior of H₂ in Aqueous Fluids under High Temperature and Pressure. *Elements: An International Magazine of Mineralogy, Geochemistry, and Petrology*, 16(1), pp.33-38.
- Beeskow, B., Treloar, P.J., Rankin, A.H., Vennemann, T.W. and Spangenberg, J., 2006. A reassessment of models for hydrocarbon generation in the Khibiny nepheline syenite complex, Kola Peninsula, Russia. *Lithos*, 91(1-4), pp.1-18

971

972 Belkhou, Rachid, Stefan Stanescu, Sufal Swaraj, Adrien Besson, Milena Ledoux, Mahdi

973 Hajlaoui, and Didier Dalle. 2015. 'HERMES: A Soft X-Ray Beamline Dedicated to X-Ray

974 Microscopy'. *Journal of Synchrotron Radiation* 22 (4): 968–79.

975

976 Bernard, C., Estrade, G., Salvi, S., Béziat, D. and Smith, M., 2020. Alkali pyroxenes and

977 amphiboles: a window on rare earth elements and other high field strength elements behavior

978 through the magmatic-hydrothermal transition of peralkaline granitic systems. *Contributions*

979 *to Mineralogy and Petrology*, 175(9), pp.1-27.

980

981 Boreham, C.J., Sohn, J.H., Cox, N., Williams, J., Hong, Z. and Kendrick, M.A., 2021.

982 Hydrogen and hydrocarbons associated with the Neoproterozoic Frog's Leg Gold Camp, Yilgarn

983 Craton, Western Australia. *Chemical Geology*, p.120098.

984

985 Bourdelle, Franck, Karim Benzerara, Olivier Beyssac, Julie Cosmidis, Daniel R. Neuville,

986 Gordon E. Brown, and Erwan Paineau. 2013. 'Quantification of the Ferric/Ferrous Iron Ratio

987 in Silicates by Scanning Transmission X-Ray Microscopy at the Fe L-2,L-3 Edges'.

988 *Contributions to Mineralogy and Petrology* 166 (2): 423–34.

989

990 Bourdelle, Franck, Teddy Parra, Olivier Beyssac, Christian Chopin, and Florent Moreau.

991 2012. 'Ultrathin Section Preparation of Phyllosilicates by Focused Ion Beam Milling for

992 Quantitative Analysis by TEM-EDX'. *Applied Clay Science* 59–60 (May): 121–30.

993

994 Chavagnac, V., Monnin, C., Ceuleneer, G., Boulart, C. and Hoareau, G., 2013.

995 Characterization of hyperalkaline fluids produced by low-temperature serpentinization of

996 mantle peridotites in the Oman and Ligurian ophiolites. *Geochemistry, Geophysics,*
997 *Geosystems*, 14(7), pp.2496-2522.

998

999 Cannat, M., Fontaine, F. and Escartin, J., 2010. Serpentinization and associated hydrogen and
1000 methane fluxes at slow spreading ridges. In *Diversity of Hydrothermal Systems on Slow*
1001 *Spreading Ocean Ridges*; Rona, P.A., Devey, C.W., Dymment, J., Murton, B.J., Eds.; AGU
1002 Geophysical Monograph Series; John Wiley and Sons: Hoboken, NJ, USA, 2010; Volume
1003 188.

1004

1005 Charlou, J.L., Donval, J.P., Fouquet, Y., Jean-Baptiste, P. and Holm, N., 2002. *Geochemistry*
1006 *of high H₂ and CH₄ vent fluids issuing from ultramafic rocks at the Rainbow hydrothermal*
1007 *field (36 14' N, MAR). Chemical geology*, 191(4), pp.345-359.

1008

1009 Chou, I.M., 1986. Permeability of precious metals to hydrogen at 2kb total pressure and
1010 elevated temperatures. *American Journal of Science*, 286(8), pp.638-658.

1011

1012 Coveney Jr, R.M., Goebel, E.D., Zeller, E.J., Dreschhoff, G.A. and Angino, E.E., 1987.
1013 Serpentinization and the origin of hydrogen gas in Kansas. *AAPG Bulletin*, 71(1), pp.39-48.

1014

1015 Decarreau A., Petit S., Vieillard P. and Dabert N., 2004. Hydrothermal synthesis of aegirine at 200 °C.
1016 *Eur. J. Mineral.*, 16, pp.85–90.

1017

1018 Donzé, F.V., Truche, L., Shekari Namin, P., Lefeuvre, N. and Bazarkina, E.F., 2020. Migration
1019 of natural hydrogen from deep-seated sources in the São Francisco Basin, Brazil.
1020 *Geosciences*, 10, p.346.

1021

1022 Drobner, E., Huber, H., Wächtershäuser, G., Rose, D. and Stetter, K.O., 1990. Pyrite
1023 formation linked with hydrogen evolution under anaerobic conditions. *Nature*, 346(6286),
1024 pp.742-744.
1025
1026 Fernandez-Prini, R., Alvarez, J.L. and Harvey, A.H., 2004. Aqueous solubility of volatile
1027 nonelectrolytes. In *Aqueous Systems at Elevated Temperatures and Pressures* (pp. 73-98).
1028 Academic Press.
1029
1030 Gaucher, E.C., 2020. New Perspectives in the Industrial Exploration for Native Hydrogen.
1031 *Elements: An International Magazine of Mineralogy, Geochemistry, and Petrology*, 16(1),
1032 pp.8-9.
1033
1034 Grozeva, N.G., Klein, F., Seewald, J.S. and Sylva, S.P., 2017. Experimental study of
1035 carbonate formation in oceanic peridotite. *Geochimica et Cosmochimica Acta*, 199, pp.264-
1036 286.
1037
1038 Gysi, A.P. and Williams-Jones, A.E., 2013. Hydrothermal mobilization of pegmatite-hosted
1039 REE and Zr at Strange Lake, Canada: A reaction path model. *Geochimica et Cosmochimica*
1040 *Acta*, 122, pp.324-352.
1041
1042 Gysi, A.P., Williams-Jones, A.E. and Collins, P., 2016. Lithogeochemical vectors for
1043 hydrothermal processes in the Strange Lake peralkaline granitic REE-Zr-Nb deposit.
1044 *Economic Geology*, 111(5), pp.1241-1276.
1045

1046 Hirose, T., Kawagucci, S. and Suzuki, K., 2011. Mechanoradical H₂ generation during
1047 simulated faulting: Implications for an earthquake-driven subsurface biosphere. *Geophysical*
1048 *research letters*, 38(17).
1049
1050 Hitchcock, Adam P. 2012. 'Soft X-Ray Imaging and Spectromicroscopy'. In *Handbook of*
1051 *Nanoscopy*, edited by Gustaaf Van Tendeloo, Dirk Van Dyck, and Stephen J. Pennycook,
1052 745–91. Weinheim, Germany: Wiley-VCH Verlag GmbH & Co. KGaA.
1053
1054 Ikorskiy, S.V., 1986. Methods of examining the compositions of gases in closed microjoints
1055 in Khibiny-intrusion rocks. *Geochem. Int.* 7, 70–74
1056
1057 Jarosewich, E. J., Nelen, J. A. & Norberg, J. A. (1980). Reference samples for electron
1058 microprobe analysis. *Geostandards Newsletter* 4, 4347
1059
1060 Klein, F., Bach, W. and McCollom, T.M., 2013. Compositional controls on hydrogen
1061 generation during serpentinization of ultramafic rocks. *Lithos*, 178, pp.55-69.
1062
1063 Klein, F., Bach, W., Humphris, S.E., Kahl, W.A., Jöns, N., Moskowitz, B. and Berquó, T.S.,
1064 2014. Magnetite in seafloor serpentinite—Some like it hot. *Geology*, 42(2), pp.135-138.
1065
1066 Klein, F., Grozeva, N.G., Seewald, J.S., McCollom, T.M., Humphris, S.E., Moskowitz, B.,
1067 Berquó, T.S. and Kahl, W.A., 2015. Experimental constraints on fluid-rock reactions during
1068 incipient serpentinization of harzburgite. *American Mineralogist*, 100(4), pp.991-1002.
1069

1070 Klein, F., Tarnas, J.D. and Bach, W., 2020. Abiotic sources of molecular hydrogen on Earth.
1071 Elements: An International Magazine of Mineralogy, Geochemistry, and Petrology, 16(1),
1072 pp.19-24.
1073

1074 Konnerup-Madsen, J., Dubessy, J., Rose-Hansen, J., 1985. Combined Raman microprobe
1075 spectrometry and microthermometry of fluid inclusions in minerals from igneous rocks of the
1076 Gardar Province (South Greenland). Lithos 18, 271–280.
1077

1078 Konnerup-Madsen, J., 2001. A review of the composition and evolution of hydrocarbon gases
1079 during solidification of the Ilímaussaq complex, South Greenland. Geol. Greenl. Surv. Bull.
1080 190, 163–170.
1081

1082 Krumrei, T.V., Pernicka, E., Kaliwoda, M., Markl, G., 2007. Volatiles in a peralkaline
1083 system: Abiogenic hydrocarbons and F–Cl–Br systematics in the naujaite of the Ilímaussaq
1084 intrusion, South Greenland. Lithos 95, 298–314.
1085

1086 Lamadrid, H.M., Rimstidt, J.D., Schwarzenbach, E.M., Klein, F., Ulrich, S., Dolocan, A. and
1087 Bodnar, R.J., 2017. Effect of water activity on rates of serpentinization of olivine. Nature
1088 communications, 8(1), pp.1-9.
1089

1090 Li, X., Zhang, C., Behrens, H., and Holtz, F., 2020. Calculating amphibole formula from
1091 electron microprobe analysis data using a machine learning method based on principal
1092 components regression. Lithos, 105469.
1093

1094 Lin, L.H., Slater, G.F., Sherwood-Lollar, B.S., Lacrampe-Couloume, G. and Onstott, T.C.,
1095 2005. The yield and isotopic composition of radiolytic H₂, a potential energy source for the
1096 deep subsurface biosphere. *Geochimica et Cosmochimica Acta*, 69(4), pp.893-903.
1097
1098 Malvoisin, B., Brunet, F., Carlut, J., Montes-Hernandez, G., Findling, N., Lanson, M., Vidal,
1099 O., Bottero, J.Y. and Goffé, B., 2013. High-purity hydrogen gas from the reaction between
1100 BOF steel slag and water in the 473–673 K range. *International journal of hydrogen energy*,
1101 38(18), pp.7382-7393.
1102
1103 Marks, M.A.W., Markl, G., 2017. A global review on agpaitic rocks. *Earth-Sci. Rev.* 173,
1104 229–258.
1105
1106 McCollom, T.M., Klein, F., Robbins, M., Moskowitz, B., Berquó, T.S., Jöns, N., Bach, W.
1107 and Templeton, A., 2016. Temperature trends for reaction rates, hydrogen generation, and
1108 partitioning of iron during experimental serpentinization of olivine. *Geochimica et*
1109 *Cosmochimica Acta*, 181, pp.175-200.
1110
1111 McCollom, T.M., Klein, F., Moskowitz, B., Berquó, T.S., Bach, W. and Templeton, A.S.,
1112 2020a. Hydrogen Generation and Iron Partitioning During Experimental Serpentinization of
1113 an Olivine–Pyroxene Mixture. *Geochimica et Cosmochimica Acta*, 282, pp. 55-75.
1114
1115 McCollom, T.M., Klein, F., Solheid, P. and Moskowitz, B., 2020b. The effect of pH on rates
1116 of reaction and hydrogen generation during serpentinization. *Philosophical Transactions of*
1117 *the Royal Society A*, 378(2165), p.20180428.
1118

1119 Ménez, B., 2020. Abiotic hydrogen and methane: Fuels for life. *Elements: An International*
1120 *Magazine of Mineralogy, Geochemistry, and Petrology*, 16(1), pp.39-46.
1121

1122 Milesi, V., Guyot, F., Brunet, F., Richard, L., Recham, N., Benedetti, M., Dairou, J. and
1123 Prinzhofer, A., 2015. Formation of CO₂, H₂ and condensed carbon from siderite dissolution in
1124 the 200–300 C range and at 50 MPa. *Geochimica et Cosmochimica Acta*, 154, pp.201-211.
1125

1126 Murray, J., Clément, A., Fritz, B., Schmittbuhl, J., Bordmann, V. and Fleury, J.M., 2020.
1127 Abiotic hydrogen generation from biotite-rich granite: A case study of the Soultz-sous-Forêts
1128 geothermal site, France. *Applied Geochemistry*, p.104631.
1129

1130 Neal, C. and Stanger, G., 1983. Hydrogen generation from mantle source rocks in Oman.
1131 *Earth and Planetary Science Letters*, 66, pp.315-320.
1132

1133 Nivin, V.A., Devirts, A.L., Lagutina, Y.P., 1995. The origin of the gas phase in the Lovozero
1134 massif based on hydrogen-isotope data. *Geochem. Int.* 32, 65–71.
1135

1136 Nivin, V.A., Belov, N.I., Treloar, P.J., Timofeyev, V.V., 2001. Relationship between gas
1137 geochemistry and release rates and the stressed state of igneous rock massifs. *Tectonophysics*
1138 336, 233–244.
1139

1140 Nivin, V.A., 2016. Free hydrogen-hydrocarbon gases from the Lovozero loparite deposit
1141 (Kola Peninsula, NW Russia). *Applied Geochemistry*, 74, pp.44-55.
1142

1143 Nivin, V.A., 2019. Occurrence forms, composition, distribution, origin and potential hazard
 1144 of natural hydrogen–hydrocarbon gases in ore deposits of the Khibiny and Lovozero Massifs:
 1145 a review. *Minerals*, 9(9), p.535.
 1146

1147 Nivin, V., 2020. The Origin of Hydrocarbon Gases in the Lovozero Nepheline-Syenite Massif
 1148 (Kola Peninsula, NW Russia), as Revealed from He and Ar Isotope Evidence. *Minerals*,
 1149 10(9), p.830.
 1150

1151 Potter, J., Konnerup-Madsen, J., 2003. A review of the occurrence and origin of abiogenic
 1152 hydrocarbons in igneous rocks. In: Petford, N., McCaffrey, K.J.W. (Eds.), *Hydrocarbons in*
 1153 *Crystalline Rocks*. Geol. Soc. Lon. Spec. Pub., vol. 214, pp. 151–173.
 1154

1155 Potter, J., Rankin, A.H. and Treloar, P.J., 2004. Abiogenic Fischer–Tropsch synthesis of
 1156 hydrocarbons in alkaline igneous rocks; fluid inclusion, textural and isotopic evidence from
 1157 the Lovozero complex, NW Russia. *Lithos*, 75(3-4), pp.311-330.
 1158

1159 Potter, J., Salvi, S. and Longstaffe, F.J., 2013. Abiogenic hydrocarbon isotopic signatures in
 1160 granitic rocks: Identifying pathways of formation. *Lithos*, 182, pp.114-124.
 1161

1162 Raabe, J., G. Tzvetkov, U. Flechsig, M. Boege, A. Jaggi, B. Sarafimov, M. G. C. Vernooij, et
 1163 al., 2008. ‘PolLux: A New Facility for Soft X-Ray Spectromicroscopy at the Swiss Light
 1164 Source’. *Review of Scientific Instruments* 79 (11): 113704.
 1165 <https://doi.org/10.1063/1.3021472>.
 1166

1167 Salvi, S., Williams-Jones, A.E., 1992. Reduced orthomagmatic C–O–H–N–NaCl fluids in the
1168 Strange Lake rare-metal granitic complex, Quebec/Labrador, Canada. *European Journal of*
1169 *Mineralogy* 4, 1155–1174.
1170
1171 Salvi, S., Williams-Jones, A.E., 1997. Fischer–Tropsch synthesis of hydrocarbons during sub-
1172 solidus alteration of the Strange Lake peralkaline granite, Quebec/Labrador, Canada.
1173 *Geochim. Cosmochim. Acta* 61, 83–99.
1174
1175 Salvi, S., Williams-Jones, A.E., 2003. Bulk analysis of volatiles in fluid inclusions. In:
1176 Samson, I.M., Anderson, A., Marshall, D. (Eds.), *Fluid Inclusions: Analysis and*
1177 *Interpretation*, Mineralogical Association of Canada, Short Course, vol. 32, pp. 247–278.
1178
1179 Salvi, S., Williams-Jones, A.E., 2006. Alteration, HFSE mineralisation and hydrocarbon
1180 formation in peralkaline systems: Insights from the Strange Lake Pluton, Canada. *Lithos* 91,
1181 19–34.
1182
1183 Seward, T.M. and Franck, E.U., 1981. The system hydrogen-water up to 440° C and 2500 bar
1184 pressure. *Berichte der Bunsengesellschaft für physikalische Chemie*, 85(1), pp.2-7.
1185
1186 Sherwood Lollar, B., Onstott, T., Lacrampe-Couloume, G. and Ballentine, C.J., 2014. The
1187 contribution of the Precambrian continental lithosphere to global H₂ production. *Nature* 516,
1188 379–382.
1189
1190 Shvarov, Y.V., 2008. HCh: new potentialities for the thermodynamic simulation of
1191 geochemical systems offered by Windows. *Geochem. Int.* 46, 834–839.

1192

1193 Siegel, K., Vasyukova, O.V. and Williams-Jones, A.E., 2018. Magmatic evolution and
1194 controls on rare metal-enrichment of the Strange Lake A-type peralkaline granitic pluton,
1195 Québec-Labrador. *Lithos*, 308, pp.34-52.

1196

1197 Sleep, N.H., Meibom, A., Fridriksson, Th., Coleman, R.G., and Bird, D.K., 2004. H₂-rich
1198 fluids from serpentinization: geochemical and biotic implications. *Proc Natl Acad Sci USA*
1199 101, 12818–12823.

1200

1201 Smith, N.J.P., Shepherd, T.J., Styles, M.T. and Williams, G.M., 2005, January. Hydrogen
1202 exploration: a review of global hydrogen accumulations and implications for prospective
1203 areas in NW Europe. In Geological Society, London, Petroleum Geology Conference series
1204 (Vol. 6, No. 1, pp. 349-358). Geological Society of London.

1205

1206 Stefánsson, A. and Seward, T.M., 2003. Stability of chloridogold (I) complexes in aqueous
1207 solutions from 300 to 600 C and from 500 to 1800 bar. *Geochimica et Cosmochimica Acta*,
1208 67(23), pp.4559-4576.

1209

1210 Prinzhofer, A., Cissé, C.S.T. and Diallo, A.B., 2018. Discovery of a large accumulation of
1211 natural hydrogen in Bourakebougou (Mali). *International Journal of Hydrogen Energy*,
1212 43(42), pp.19315-19326.

1213

1214 Truche, L., Joubert, G., Dargent, M., Martz, P., Cathelineau, M., Rigaudier, T. and Quirt, D.,
1215 2018. Clay minerals trap hydrogen in the Earth's crust: evidence from the Cigar Lake uranium
1216 deposit, Athabasca. *Earth and Planetary Science Letters*, 493, pp.186-197.

1217

1218 Truche, L. and Bazarkina, E.F., 2019. Natural hydrogen the fuel of the 21st century. In E3S
1219 Web of Conferences, 98, p. 03006. EDP Sciences.

1220

1221 Truche, L., McCollom, T.M. and Martinez, I., 2020. Hydrogen and Abiotic Hydrocarbons:
1222 Molecules that Change the World. Elements: An International Magazine of Mineralogy,
1223 Geochemistry, and Petrology, 16(1), pp.13-18.

1224

1225 Vacquand, C., Deville, E., Beaumont, V., Guyot, F., Sissmann, O., Pillot, D., Scilla, C. and
1226 Prinzhofer, A., 2018. Reduced gas seepages in ophiolitic complexes: Evidences for multiple
1227 origins of the H₂-CH₄-N₂ gas mixtures. Geochimica et Cosmochimica Acta 223, 437–461.
1228 <https://doi.org/10.1016/j.gca.2017.12.018>

1229

1230 Vasyukova, O.V., Williams-Jones, A.E. and Blamey, N.J.F., 2016. Fluid evolution in the
1231 Strange Lake granitic pluton, Canada: Implications for HFSE mobilisation. Chemical
1232 Geology, 444, pp.83-100.

1233

1234 Vasyukova, O. V., and A. E. Williams-Jones. "Closed system fluid-mineral-mediated trace
1235 element behaviour in peralkaline rare metal pegmatites: Evidence from Strange Lake."
1236 Chemical Geology 505 (2019): 86-99.

1237

1238 Worman, S.L., Pratson, L.F., Karson, J.A. and Klein, E.M., 2016. Global rate and distribution
1239 of H₂ gas produced by serpentinization within oceanic lithosphere. Geophysical Research
1240 Letters, 43(12), pp.6435-6443.

1241

1242 Worman, S.L., Pratson, L.F., Karson, J.A. and Schlesinger, W.H., 2020. Abiotic hydrogen
1243 (H₂) sources and sinks near the Mid-Ocean Ridge (MOR) with implications for the
1244 seafloor biosphere. Proceedings of the National Academy of Sciences.
1245